Review Article

On aeolian transport: Grain-scale interactions, dynamical mechanisms and scaling laws

O. Durán, P. Claudin, B. Andreotti *

Laboratoire de Physique et Mécanique des Milieux Hétérogènes (PMMH UMR 7636 CNRS – ESPCI – Univ. Paris Diderot – Univ. P. & M. Curie), 10 Rue Vauquelin, 75231 Paris Cedex 05, France

ARTICLE INFO

ABSTRACT

Aeolian processes involve the wind action on a sedimentary substrate, namely erosion, sand transport and deposition. They are responsible for the emergence of aeolian dunes and ripples but also erosive structures like yardangs. In this review, we discuss the physics of aeolian sediment transport from a physical point of view. Relevant time and length scales associated to turbulent wind fluctuations are summarized using aerodynamic theory. At the microscopic scale, the different forces acting on the grains are detailed. We then introduce the concepts – e.g. saturated flux, saturation length – and the relevant framework for the development of a continuum quantitative description of transport. Static and dynamical entrainment thresholds are modeled and discussed. Steady transport is investigated in two asymptotic regimes: close to threshold and far above it. In both cases, a simple picture, taking into account the negative feedback of particles on the wind flow, is analytically drawn and compared to experimental and numerical data. The low wind velocity regime corresponds to the model proposed by Ungar and Haff (1987) and the high wind velocity regime is elaborated from initial ideas of Bagnold (1941). Transport transient is also studied in detail, and scaling laws for the saturation length are proposed. Finally, some open issues for future research are outlined in the conclusion.

Contents

* Corresponding author.
   E-mail address: andreotti@pmmh.espci.fr (B. Andreotti).

1. Introduction

When the wind blowing over a sand bed exceeds a certain velocity threshold, the particles of the bed can be set into motion and transported away. Different modes of transport are usually classified following the nature of forces at work on the grains (Fig. 1). When hydrodynamical forces are dominant, as for fine particles, grains are transported in suspension. When the particles are large enough so that gravity is also influential, the grains experience successive jumps and the transport mode is called saltation. Larger particles (bed load) move by tractation or creep motion, where bed contact is maintained, and gravity, hydrodynamical as well as contact forces are all important. Finally, when saltation is strong enough, grains on the bed are ejected by impacts of the saltating grains and move by a small hop. This is called reptation. This mode is then dominated by gravity and contact forces. In contrast to the other modes, reptation is specific to the aeolian situation, i.e. to the case for which the density of the fluid is much smaller than that of the grains. A dense fluid such as water effectively dissipates most of the kinetic energy of the moving grains at the moment of impact. Following the nomenclature of ordinary particle physics, we have proposed to name the grains contributing to the different modes of transport: saltons, reptons, tractons and suspendons.

The qualitative understanding and the quantitative description of sand transport by wind is a major issue discussed in the aeolian community (Sarre, 1987; Pye and Tsoar, 1990; Anderson et al., 1991; McEwan and Willetts, 1993, 2000; Andreotti et al., 2002a; Nickling and McKenna Neuman, 2009; Zheng, 2009). This research area is also important in an environmental context. In particular, it governs some of the mechanisms at the heart of the formation of ripples and dunes (Fryberger and Dean, 1979; Cooke et al., 1993). Taking a definite physical point of view, we wish in this paper to review and explain all the physical ingredients that are essential to achieve this understanding. Rather than treating all of these different modes in their whole complexity, we show how the description of transport can be abstracted into a few key quantities: the entrainment threshold, the saturated flux and the saturation length and time scales. Also, avoiding empiricism as much as possible, for all involved mechanisms and limiting regimes we derive the corresponding scaling laws, in which the dominant parameters are evidenced.

We start with basics concepts of aerodynamics that are relevant to sediment transport (Section 2). We then detail the different forces acting at grain scale (Section 3). In Section 4, we introduce the concepts and the formalism for the development of a general quantitative description of transport. Section 5 is
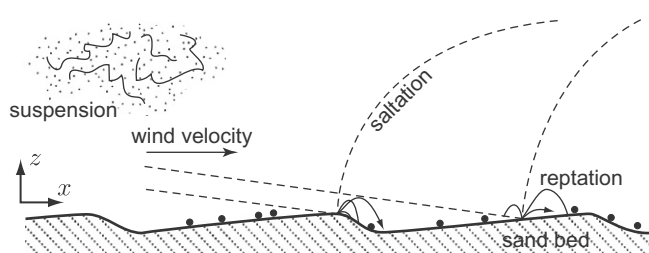
Fig. 1. Schematic representation of the different transport modes.

devoted to the description of the static and dynamic threshold. In Section 6, we present two limiting regimes of transport: close to the threshold and far above it. In both cases, a simple picture can be analytically drawn. The low wind velocity regime is elaborated from the ideas first proposed by Ungar and Haff (1987). In the high wind velocity regime, the scaling laws proposed by Bagnold (1941) are explored under a new context. Section 7 is dedicated to transport transient, and scaling laws for the saturation length are proposed. Finally, the conclusion (Section 8) is a presentation of current important and open problems that should be investigated in future research.

2. Aerodynamical time and length scales for aeolian transport

Common observation shows that the amount of sand transported increases with the wind velocity. In this section, we discuss some of the difficulties arising when one aims to relate quantitatively sand flux to velocity measurements. They are related to the key issue of determining the relevant aerodynamical time and length scales for aeolian transport.

2.1. Fluctuations of wind velocity

Aeolian transport generically takes place in a turbulent flow. Saltation is effectively related to the capacity of grains to rebound and to expel other grains when they collide the sand bed, a characteristic which disappears when the fluid viscosity v is high or when the density ratio ρ_p/ρ_f between the particles and the fluid is low. A turbulent flow is characterized by a velocity field fluctuating over a wide range of space and time-scales. The time-scale over which the forcing of the flow takes place is called the integral time scale T. It is the time difference beyond which velocities measured at a single place and at two different times become uncorrelated. Similarly, the length at which the forcing of the flow takes place is called the integral length scale L. The velocity signals measured at the same time in two points separated by a distance larger than L are uncorrelated. Using L and T, one can construct a large scale velocity $U = L/T$. Alternatively, U can be defined as the root mean square velocity fluctuations over a time window $T = L/U$.

Under natural conditions, winds result from the differential heating of geographic zones at different scales. Large scale atmospheric circulation is due to the temperature contrast between the poles and the equator, and is sensitive to the planetary Coriolis effect. Local winds can dominate in coastal zones and be influenced by topography. In deserts, the forcing scale is set by the altitude of the so-called capping inversion layer, which separates the convective boundary layer from the stable free atmosphere: L is typically on the order of 10^3 m. Sand is transported when the wind is sufficiently strong i.e. when U is on the order of 10^0 m/s. The integral time-scale T from the meteorological point of view is thus around 10^3 s, i.e. 15 min. The atmospheric Reynolds number $Re = UL/v$ is typically on the order of 10^8. In a wind tunnel, the flow is induced by a longitudinal pressure gradient (White and Mounla, 1991). Most wind tunnels are meter scale $L \sim 10^0$ m so that the Reynolds number is 'only' 10^5, for the same velocity U. The corresponding integral time-scale T is on the order of 1 s.

The velocity variations over time-scales smaller than T may be called turbulent fluctuations (Fig. 2a). The velocity variations over time-scales larger than T can be qualified as meteorological and are of a different nature (Fig. 2b). They result from a combination of randomness and coherence. In particular, the diurnal cycle and the annual seasonal cycle induce periodic deterministic components of period 1 day and 1 year, respectively. In between the meteorological range and the turbulent range of the temporal spectrum, wind velocity signals show a spectral gap where the fluctuations are small (Van der Hoven, 1957; Harris, 2008). Weather is controlled by atmospheric structures whose horizontal length-scale is around 10^7 m and whose velocity is around 10^1 m/s. The associated time-scale, which is around 10 days, gives
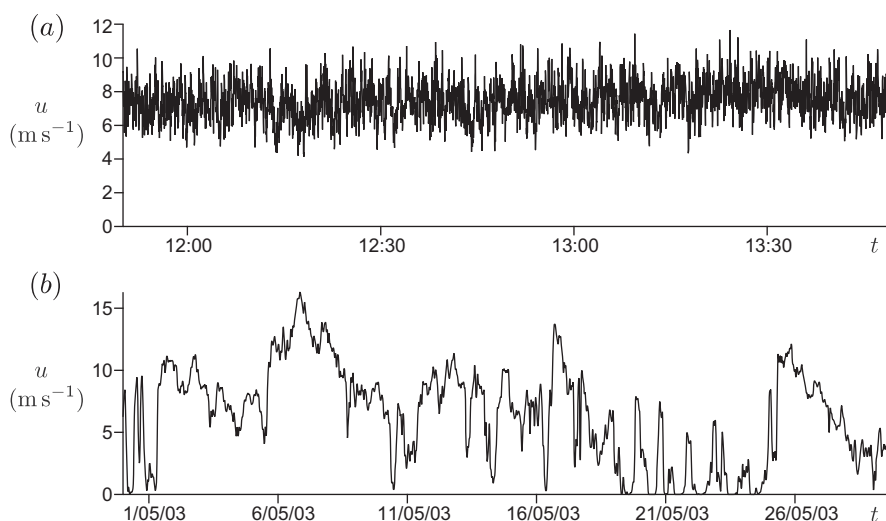
Fig. 2. The two types of wind velocity time variations. (a) Turbulent fluctuations of the wind velocity, measured with an anemometer whose response time is $\simeq 1$ s. This corresponds to the time-scale T_{drag} at which grains respond. Two hours of signal are represented, during which the wind conditions – the wind velocity averaged over the turbulent integral time-scale T – were constant. Still, the fluid velocity averaged at the time-scale T_{drag} and therefore the sediment flux present fluctuations. (b) Typical variations of the wind velocity at the turbulent integral scale T. The same anemometer is used, but the velocity is averaged over a 15 min time-window. The date is shown in little endian form.
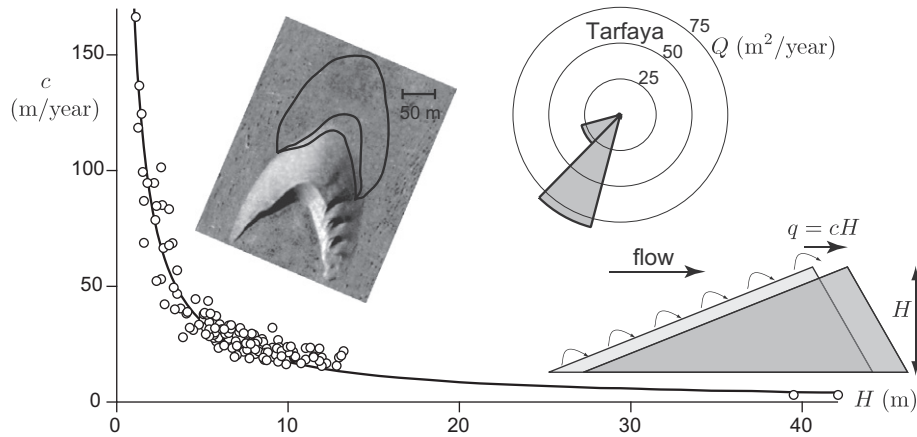
Fig. 3. Relation between dune speed c and height H measured for aeolian barchans of the Atlantic Sahara (○). The solid line is Bagnold's expression: $c \propto Q/H$. As shown by the photograph the distance between the position of a Barchan dune at two dates is measured using both aerial photographs and GPS contours. Flux rose: saturated flux over a flat bed Q computed from wind velocity measurements in Tarfaya (Atlantic Sahara) as a function of the wind direction. This flux rose is aligned with the dune propagation velocity. Data from Elbelrhiti et al. (2005, 2008).

the lower bound of the climate range of time-scales. We note for completeness that different authors (see Lovejoy and Schertzer (2010) for a recent review) challenge the existence of the spectral gap associated to the 2D/3D transition and claims the existence of a unique cascade across time T.

The statistical properties of turbulent fluctuations are determined by the forcing velocity, i.e. the velocity averaged over a time-window T. As a consequence, the sediment transport is expected to be correlated with the wind strength, when both are averaged over the time-scale T. Cup-anemometers with a sampling time around 0.1 Hz are thus perfectly adapted to characterize average sand transport. Airport weather stations with 4 or 24 measurements a day may even be sufficient. For example, Fig. 3 shows the relation between propagation speed c of dunes, their height H and the saturated flux over a flat bed Q, which is determined from the wind velocity averaged over T. The typical time-scale to measure significant barchan displacements is several years (Finkel, 1959; Long and Sharp, 1964; Hastenrath, 1967, 1987; Slattery, 1990) or several decades for the 40 m high mega-bachans. The observed agreement with Bagnold's relation $c \propto Q/H$ supports the assumptions that dune slip faces can be considered perfect sand traps (see schematic in Fig. 3) and that the mean wind velocity is the relevant information needed to determine the mean sand flux.

The finest scales of turbulence must be resolved to enable experimental measurement of turbulent velocity fluctuations. The velocity fluctuations $\delta u(\ell)$ at scale ℓ are on the order of $U(\ell/L)^{1/3}$ (Kolmogorov, 1941; Frisch, 1996). The local Reynolds number $\ell\delta u(\ell)/\nu$, which characterizes the motion at scale ℓ, reaches 1 at the so-called Kolmogorov scale ℓ_K, which scales as $LRe^{-3/4}$. The corresponding time-scale $\ell_K/\delta u(\ell_K)$ scales as TRe^{-1}. For atmospheric turbulence, the Kolmogorov length-scale ℓ_K is millimetric and the time-scale is around 10^{-1} s. For a wind tunnel, the Kolmogorov time-scale can be much smaller (between 10^{-3} and 10^{-2} s). Hot wire anemometers exhibit these ideal space and time resolutions.

Following Reynolds' decomposition principle, the full velocity field can be decomposed into average u_i and fluctuating u_i' components. By construction, the variations of the average are slower than T and those of the fluctuations faster than T. This decomposition can be performed by applying a low-pass/high-pass filtering at frequency T^{-1}, for instance by averaging over a time-window T. The equations governing the average velocity field u_i can be written as:

$$\partial_i u_i = 0, \tag{1}$$
$$\rho_f D_t u_i = \rho_f \left(\partial_t u_i + u_j \partial_j u_i \right) = -\partial_j \tau_{ij} - \partial_i p, \tag{2}$$

where $\tau_{ij} = \rho_f \langle u_i' u_j' \rangle$ is the Reynolds stress tensor, defined as the low-pass filtering of the product of velocity fluctuations (both $\langle u_i' \rangle$ and $\langle u_j' \rangle$ must be zero). The Reynolds stress is an inertial effect interpreted as a pseudo-stress tensor. The turbulent shear stress is defined as: $\tau_{xz} = \rho_f \langle u_x' u_z' \rangle$. It is a vertical flux of horizontal momentum carried by wind fluctuations. As exemplified below, the averaging procedure must be consistent with the time-scales of the problem. In particular, the instantaneous value of $u_i' u_j'$ is *not* an instantaneous shear stress.

2.2. Turbulent boundary layer

The wind flow above a sand bed is called the turbulent boundary layer. We first consider a flat homogeneous ground, where the shear stress is a constant, noted $\rho_f u_*^2$, where u_* is called the shear velocity. The flux of momentum is transmitted from the upper layers of the atmosphere to the ground throughout air. The turbulent regime is characterized by the absence of any intrinsic length and time scales. In particular, the viscosity is completely inefficient at large scales. At a sufficiently large distance z from the ground (but $z \ll L$), the only length-scale limiting the size of turbulent eddies – the so-called mixing length – is precisely z and the only mixing time-scale is given by the velocity gradient $|\partial_z u_x|$. As originally shown by Prandtl (1925), it results from this dimensional analysis that the only way to construct a diffusive flux is a turbulent closure of the form:

$$\tau_{xz} = -\kappa^2 \rho_f L^2 |\partial_z u_x| \partial_z u_x, \tag{3}$$

where the mixing length is $L = z$ and $\kappa \simeq 0.4$ is the (phenomenological) von Kármán constant. In the logarithmic boundary layer, the normal stresses can be written as:

$$\tau_{xx} = \tau_{yy} = \tau_{zz} = \frac{1}{3}\tau_{ll} \quad \text{with} \quad \tau_{ll} = \kappa^2 \chi^2 \rho_f L^2 |\partial_z u_x|^2, \tag{4}$$

where χ is a second phenomenological constant estimated in the range 2.5–3. Note that χ does not have any influence as it describes the isotropic component of the Reynolds stress tensor, which can be absorbed into the pressure terms. Introducing the strain rate tensor $\dot{\gamma}_{ij} = \partial_i u_j + \partial_j u_i$ and its squared modulus $|\dot{\gamma}|^2 = \frac{1}{2}\dot{\gamma}_{ij}\dot{\gamma}_{ij}$, we can write both expressions (3) and (4) in a general tensorial form:

$$\tau_{ij} = \kappa^2 \rho_f L^2 |\dot{\gamma}| \left(\frac{1}{3}\chi^2 |\dot{\gamma}|\delta_{ij} - \dot{\gamma}_{ij} \right). \tag{5}$$

As the shear stress is constant across the turbulent boundary layer, one obtains the velocity by a simple integration. It has a single non-zero component along the *x*-axis, which increases logarithmically with z (Stull, 1988; Garrat, 1994):

$$u_x = \frac{u_*}{\kappa} \ln\left(\frac{z}{z_0}\right), \tag{6}$$

where z_0 is a constant of integration called the aero/hydrodynamic roughness.

This expression does not apply for $z \to 0$: close to the bottom, there is a so-called surface layer, which matches the logarithmic profile to a null velocity on the ground. The hydrodynamic roughness z_0 should be distinguished from the geometrical (or physical) roughness of the ground, usually defined as the root mean square of the height profile variations. z_0 is defined as the height at which the velocity would be zero, when extrapolating the logarithmic profile (6) to small z. There are number of physical mechanisms that control z_0. If the ground is smooth enough, a viscous sub-layer of typical size $\mathcal{O}(\nu/u_*)$ exists, whose matching logarithmic profile determines the value of z_0. On the contrary, if the geometrical roughness is larger than the viscous sub-layer, turbulent mixing dominates at small z with a mixing length controlled by the ground topography. In the case of a static granular bed composed of grains of size d, reported values of the hydrodynamic roughness are reasonably consistent: $z_0 \simeq d/30$ in Bagnold (1941), $z_0 \simeq d/24$ in Schlichting and Gersten (2000) and $z_0 \simeq d/10$ in Kamphuis (1974) and Andreotti (2004). The situation is different in the presence of sediment transport, which induces a negative feedback on the flow. In this case, the hydrodynamic roughness z_0 may be directly controlled by the transport characteristics (e.g. mass flux and grain trajectories), see Sections 6.1.3 and 6.4.

Finally, it is worth noting that there is a factor $\simeq 35$ between the wind velocity measured at 10 m above the ground and u_*. A shear velocity value of 1 m/s corresponds to a wind blowing at 125 km/h 10 m above the surface.

2.3. Fluctuations of sediment transport

Due to inertia, the motion of sand grains responds very differently to small and large time-scale velocity fluctuations. The length needed to accelerate a grain at the wind velocity U (see Eq. (61)) is called the drag length L_{drag} and scales as

$$L_{\mathrm{drag}} \simeq 2\frac{\rho_p}{\rho_f}d. \tag{7}$$

It is on the order of 1 m. The associated time-scale is

$$T_{\mathrm{drag}} = \frac{L_{\mathrm{drag}}}{U} \simeq 2\frac{\rho_p}{\rho_f}\frac{d}{U} \tag{8}$$

and is on the order of 1 s. To characterize aeolian sediment transport, one usually defines a sand flux by averaging over the motion of many grains. T_{drag} and L_{drag} are the relevant scales to perform such averaging as the flux cannot evolve more rapidly than T_{drag} and over distances smaller than L_{drag}. The vertical scale is set by the transport layer thickness H_f, which is on the order of 10^{-2} m.

In a wind tunnel, T_{drag} coincides with the integral time-scale T. As a consequence, the sand transport (averaged over a time T_{drag}) does not fluctuate much. Conversely, in the field, T_{drag} is much smaller than T so that sand transport fluctuation is high. Since these fluctuations are part of the turbulence, they are statistically determined by the wind velocity, if the later is properly averaged over the integral time T. At this time-scale, the sand transport is well and truly a function of the wind velocity. A striking consequence of this property occurs in the field when one tries to relate sand transport to velocity signals. If the distance between the flux

and velocity sensors is too large, they dot not sample the same turbulent structures and so their signals do not correlate with any fluctuations. However, their correlation can be restored by averaging the signals over a time window of size T.

The situation in which the transport law is calibrated is usually a uniform turbulent boundary layer of constant shear velocity u_* over a flat sand bed. In this situation, one observes a steady uniform transport characterized by a flux q_{sat} called the saturated flux, which corresponds to an equilibrium between flow and transport. q_{sat} is an increasing function of u_*. As u_* must be defined at the integral time-scale T, the curves $q_{\mathrm{sat}}(u_*)$ obtained in a wind tunnel and in the field may be quantitatively different although qualitatively similar.

In order to relate them to each other we must consider T_{drag}. Transport is mostly determined by the velocity field inside the transport layer. The time-scale over which the momentum is exchanged in the fluid increases linearly with the distance z from the surface as z/u_*. The equilibration time of the fluid inside the transport layer is then on the order of $H_f/u_* \sim 10^{-2}$ s, which is much smaller than T_{drag}. In the atmospheric case, one can thus construct a time-varying shear velocity u_*, measured at the level of the transport layer, and averaged over T_{drag}. The relation between the sand flux, also averaged over T_{drag}, and this shear velocity should in principle be the same as that measured in a wind tunnel. By a further averaging of the relation over the integral time T, one obtains the relation valid at this atmospheric time-scale.

2.4. Turbulent flow over a relief

As shown by Jackson and Hunt (1975), the turbulent flow over an undulating topography of wavelength λ and with a small aspect ratio can be decomposed into three regions.

- *Outer layer:* In the outer layer, away from the bottom, the pressure gradient is mostly balanced by inertial terms, like in an inviscid potential flow. The streamlines follow the topography so that the velocity at the bottom of the outer layer is in phase with the bottom, i.e. it is largest above the crests of the bumps.
- *Inner layer:* In the inner layer, the inertial terms of the Navier–Stokes equation are negligible, and the longitudinal pressure gradient is thus balanced by the Reynolds shear stress transverse gradient i.e. by the mixing of momentum due to turbulent fluctuations. The thickness ℓ of the inner layer is related to the wavelength by $\lambda \sim \ell\ln^2(\ell/z_0)$. At the transition between the inner and outer layers, the fluid velocity is slowed down by the shear stress. Due to inertia, when a stress is applied, the velocity response is lagged. Then, the velocity, which is inherited from the outer layer is always phase delayed with respect to the shear stress. As a consequence, the shear stress is phase-advanced with respect to the topography, which means that the shear stress reaches its maximum upstream of the crests of the bumps. The shear stress phase shift vanishes for asymptotically small z_0/λ and gently increases with $\ln(z_0/\lambda)$ (Fourrière et al., 2010). The asymptotic calculation performed by Jackson and Hunt (1975) and simplified by Kroy et al. (2002a,b) is recovered only for asymptotically large $\ln(\lambda/z_0)$, a limit rarely reached in real problems.
- *Surface layer:* The surface layer, already introduced, is responsible for the hydrodynamical roughness z_0 seen from the inner layer. The shear stress profile is insensitive to the mechanisms at work in the surface layer, provided that its thickness is smaller than that of the inner layer: the hydrodynamical roughness is then the single quantity inherited from the surface layer.

This structure has very important consequences for sand transport and wind velocity measurements. First, as the wind strength

varies along the dune topography, the sand flux is never saturated. We will develop in Section 4.4 a framework which accounts for saturation transients. Second, the velocity profile in the outer layer is not logarithmic. Therefore, one cannot extract the local value of the shear velocity at the surface of a dune from the fit of the velocity profile to relation (6), which is only valid in homogeneous situations.

Still, one can use the relation between the saturated flux and the basal shear velocity if the transport layer is embedded in the inner layer ($H_f < \ell$). For this, the basal shear velocity u_* must be determined from velocity measurements performed inside this inner layer. In practice, for a dune of length λ, the sensors have to be placed within a distance $\simeq 10^{-2}\lambda$ from the bed. The easiest method is to place an anemometer just above the transport layer, where the shear velocity is the measured velocity multiplied by a constant factor. For quantitative applications, it is necessary to calibrate the relation between the roughness z_0 and the velocity in a wind tunnel.

3. Force acting on grains

The aim of this section is to review the different forces at work at the scale of grains. We start with aerodynamical forces, then treat contact forces between grains, and finally describe the collision between two particles. As stated in Section 1, the nature of these forces determines the classification of the modes of transport. These forces are also important for threshold scaling laws. Further, this analysis provides the microscopic input for subsequent discrete or continuum descriptions, and at the end of this section we describe the principle of discrete element numerical simulations for sediment transport. We focus on basic results in this section and provide more details in Appendix A.

3.1. Aerodynamic forces in uniform steady flows

3.1.1. Viscous regime

Consider a grain of diameter d moving at a constant speed $\vec{u}^p$ with respect to a steady fluid of density ρ_f and viscosity η (Fig. 4a). The dynamics are controlled by a single non-dimensional number, the grain-based Reynolds number $\mathcal{R}$, which compares inertial and viscous effects at the scale of the grain:

$$\mathcal{R} = \frac{\rho_f u^p d}{\eta} = \frac{u^p d}{v}, \tag{9}$$

where $v = \eta/\rho_f$ is the kinematic viscosity.

At low Reynolds number $\mathcal{R}$, exchanges of momentum between the grain and the fluid are dominated by viscous diffusion. The drag force exerted by the fluid on the grain, which results from viscous shear stress, can be estimated dimensionally. As the velocity gradient is proportional to u^p/d, the viscous stress scales as $\eta u^p/d$. The surface on which this stress is applied is proportional to d^2. The force exerted by the fluid on the particle is simply the stress multiplied by the surface:

$$\vec{F}_d \sim -\eta d\vec{u}^p. \tag{10}$$

It is possible to compute this force exactly, for the case of a sphere with diameter d. Given a sphere area of πd^2, the numerical coefficient in front of expression (10) is then equal to 3π, so that the drag force, called the Stokes force in this case, reads:

$$\vec{F}_d = -3\pi\eta d\vec{u}^p. \tag{11}$$

Given this low Reynolds number limit, the velocity field around a moving particle decreases by $1/r$, where r is the distance to the particle center. This slow decrease explains the long range interactions between grains in a viscous suspension. Let us apply the Stokes formula to sediments. Consider a unique spherical falling grain subjected to gravity. The force balance reads

$$\vec{F}_d = \frac{\pi}{6}(\rho_p - \rho_f)d^3\vec{g} \tag{12}$$

and the fall velocity is defined as

$$u_{\text{fall}} = \frac{\rho_p - \rho_f}{\rho_f}\frac{gd^2}{18v}. \tag{13}$$

3.1.2. Turbulent regime

At high Reynolds number, the viscous diffusion is negligible relative to the convective transport due to velocity fluctuations. The force $\vec{F}_d$ exerted on a spherical grain remains parallel to the velocity $\vec{u}^p$ but does not depend anymore on viscosity. The main force results from the asymmetry of pressure between the two sides of the grain (Fig. 4c). As the streamlines converge along the upstream face of the grain, this zone of the flow does not fluctuate much, so that energy dissipation is low there. One can apply Bernoulli relation to estimate the pressure on the upstream side of the grain as $\frac{1}{2}\rho_f u^{p2}$. On the grain flanks, the boundary layer separates from the grain and a highly dissipative recirculation bubble forms. The pressure on the downstream face is thus negligible. Globally, the total force is on the order of the product of the pressure by the surface

$$\vec{F}_d = -\frac{\pi}{8}C_\infty \rho_f d^2 u^p\vec{u}^p. \tag{14}$$

The factor C_∞ is called the drag coefficient and depends on the grain shape. For smooth spheres, at high Reynolds number, the experimental value of C_∞ is approximately 0.47 but for natural grains, physical measurements indicate $C_\infty \simeq 1$.

In the turbulent regime, the fall velocity becomes:

$$u_{\text{fall}} = \sqrt{\frac{\rho_p - \rho_f}{\rho_f}\frac{4gd}{3C_\infty}}. \tag{15}$$

Let us consider quartz grains, 300 μm in diameter, falling down through air. Their terminal velocity is on the order of 3 m/s, which is a few times greater than the typical velocity of grains transported in saltation by the wind, when they collide with the ground. In this example, the particle Reynolds number is only 60, which means that grains in saltation are in the cross-over between the regime dominated by viscous stress and that dominated by the downwind/upwind asymmetry of the pressure field. The same is true for saltons on Mars, Venus or Titan, with $\mathcal{R}$ on the order of 10.

3.1.3. Cross-over between the two regimes

It may be of interest, for practical reasons, to describe the two above asymptotic regimes by a unique law. From dimensional analysis, the resultant of hydrodynamical forces acting on a grain keep the form:

$$\vec{F}_d = -\frac{\pi}{8}C_d(\mathcal{R})\rho_f d^2 u^p\vec{u}^p. \tag{16}$$

The drag coefficient C_d is now a function of the Reynolds number $\mathcal{R}$, which can be determined experimentally. At low Reynolds number,
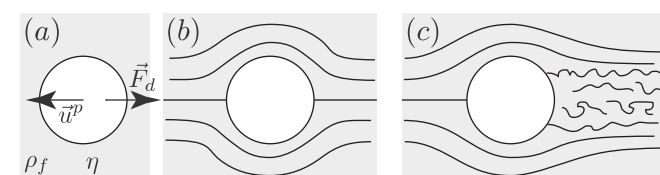
Fig. 4. (a) Schematic of a grain moving at the velocity $\vec{u}^p$ in a fluid at rest. (b) Streamlines in the frame of reference of the grain, in the viscous regime ($\mathcal{R} \ll 1$) and (c) in the inertial regime ($\mathcal{R} \gg 1$).

the force is proportional to the viscosity, which means that C_d must be proportional to $\mathcal{R}^{-1}$. At high Reynolds number, the drag coefficient tends to the constant C_∞ defined above. To match these two scaling laws, the following empirical formula is satisfactory

$$C_d = \left(C_\infty^{1/2} + s\mathcal{R}^{-1/2}\right)^2, \tag{17}$$

where s is a constant on the order of $\simeq \sqrt{24} \simeq 5$ (Ferguson and Church, 2004). Note that, this relation does not account for the so-called drag crisis, for which C_d shows a sharp decrease between $\mathcal{R} = 10^5$ and $\mathcal{R} = 10^6$, i.e. well above values encountered in natural aeolian situations.

3.2. Aerodynamical forces in unsteady heterogeneous flows

In the previous paragraph, we have considered a single grain at a constant speed with respect to a fluid at rest. In most cases, however, the grains are in motion in an unsteady inhomogeneous fluid. What are the hydrodynamical forces acting on a particle in this situation? In the limit of small Reynolds numbers, it is possible to perform analytical developments from the viscous regime, taking into account various effects at the perturbative order: unsteadiness, inertial effects, velocity gradient influence, etc. However, measurements show that these systematic developments have a small range of validity: above a Reynolds number of order 10, the discrepancies with perturbative analysis is such that one has to go back to dimensional analysis. In the limit of high Reynolds number flows, there is no such asymptotic developments. A common trick is to keep the same expression as above, but replace the grain velocity $\vec{u}^p$ by the relative velocity $\vec{u}^p - \vec{u}$. This is rigorous given the condition that the fluid should not present any intrinsic fluctuation. However, the hydrodynamical forces result from not only the fluctuations induced by the grain, but also those due to the flow turbulence. Very few results exist on the forces felt by one grain whose size would be in the inertial range of a turbulent flow. A number of examples are described in Appendix A.

3.3. Contact forces and collisions

In this subsection, we describe the forces exerted by two grains in contact as well as collisions between grains (Fig. 5). In particular, we address the microscopic and geometrical contributions to the macroscopic laws of solid friction. We also describe the physics at work during the collision of two grains. In the context of aeolian transport, this section is particularly relevant for the description of a granular bed, as well as the collision of grains on the bed.

3.3.1. Hertz elastic contact

Let us first consider the normal force $\vec{N}$ resulting from the overlap 2δ of two spherical grains in contact (Fig. 5a). This force results from the elastic repulsion inside the contact zone. For geometrical reasons, this zone has a radius $a \simeq \sqrt{\delta d}$. The strain generated by this compression is on the order of δ/a, so that the force is
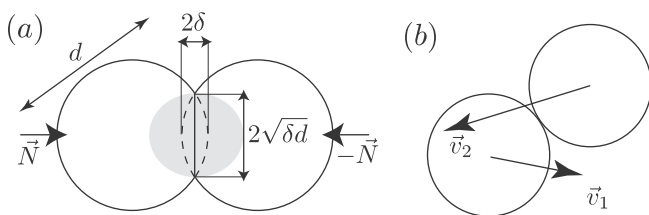
$N \simeq E\delta/a \times a^2$, where E is the Young modulus. The exact derivation of the sphere–sphere contact (Johnson, 1985; Landau and Lifchitz, 1990) gives:

$$N = \frac{E\sqrt{d}}{3\left(1 - v_p^2\right)} \delta^{3/2}, \tag{18}$$

where v_p is the Poisson coefficient of the material the spheres are made of. Note that this force is non-linear with respect to the overlap: the contact becomes harder as one pushes more.

3.3.2. Solid friction laws

Two touching grains also exhibit a tangential force coming from the friction of the surfaces in contact. The macroscopic laws controlling the friction between two solids have been formalized by Amontons (1699) and Coulomb (1773) as follows (see Fig. 6a for notations). Starting from rest, the norm of the tangential reaction have to reach the value $|\vec{R}_T| = \mu_s|\vec{R}_N|$ to initiate the motion. μ_s is called the static friction coefficient between the two solids. If there is no motion, $\vec{R}_T$ is undetermined and only the inequality $|\vec{R}_T| \leqslant \mu_s|\vec{R}_N|$ holds. Once the block moves, the friction force is oriented in the direction opposed to that of the motion and its norm is $|\vec{R}_T| = \mu_d|\vec{R}_N|$, where $\mu_d < \mu_s$ is now the dynamic friction coefficient. The coefficients μ_s and μ_d are phenomenological constants that depend on the nature of the materials in contact. Typical values are $1 > \mu_s > \mu_d > 0.1$. For convenience, one can use alternative friction angles α defined as $\tan\alpha = \mu$.

The Amontons–Coulomb law is particularly simple and robust and is widely used for practical purposes. Its microscopic origin has been elucidated by Bowden and Tabor (1950). Furthermore, as shown in Fig. 6b, most solid surfaces are not smooth but have microscopic roughness, and the contact between two solids takes place at the level of the largest asperities. The real surface of contact, A_{real}, is thus much smaller than the apparent, macroscopic one, A_{apparent}. The stress at the level of the micro-contact is larger than the macroscopic stress by a factor $A_{\text{real}}/A_{\text{apparent}}$, which is typically around 10^3. The normal stress is so large that the material deforms plastically until it reaches the hardness of the material H. Then, the real contact surface becomes directly proportional to the normal load: $HA_{\text{real}} = |\vec{R}_N|$. The macroscopic friction law can then be explained by the rheology of the material in the micro-contacts. Sliding of the micro-contacts under shear occurs when the tangential stress $|\vec{R}_T|/A_{\text{real}}$ exceeds the yield stress σ_Y of the material. Finally, by combining the two relations, a microscopic friction coefficient is determined by $\mu = \sigma_Y/H$.

3.3.3. Effective friction of granular matter

Granular assemblies also follow solid friction laws. However, this behavior takes place at a much larger scale than the contact between grains. The effective friction coefficient results both from the friction in the microscopic contact asperities discussed above, and from the geometrical tangle of the grains. Consider the simple granular packing of Fig. 7b. In this case, the upper grain can be set

Fig. 5. (a) Elastic contact between two spheres of diameter d, pushed one against the other by a distance 2δ. The strain is localized over the gray zone of size a. (b) Inelastic collision between two spheres approaching at velocities $\vec{v}_1$ and $\vec{v}_2$.
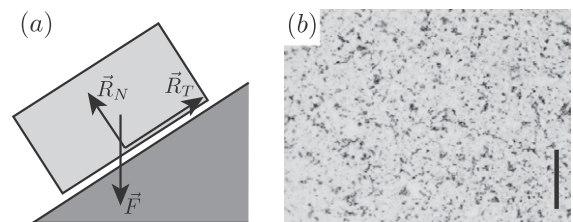

Fig. 6. (a) Schematics of Amontons–Coulomb's laws of friction. (b) Transmission electron microscopy picture of the interface between two blocks of epoxy resin (photo credit: Ronsin). Contacts appear in black. Scale bar: 100 μm.
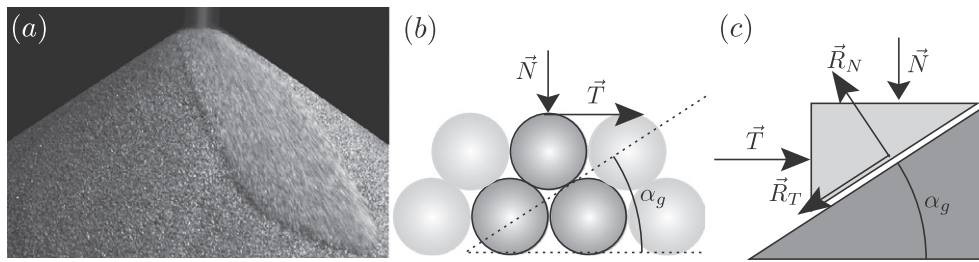
Fig. 7. (a) Photograph of a sand avalanche at the surface of a sand pile. Avalanches nucleate when the slope is locally larger than the static friction coefficient μ_s. They stop when the slope has reached the dynamic friction coefficient. (b) Schematic showing the angle α_g of the direction along which the upper grain starts moving when T is large enough. (c) The effective friction results from the microscopic friction coefficient and from the packing geometry.

into motion if it moves over the neighboring grain. This is formally similar to the sliding of a block along a solid plane inclined at an angle α_g, which reflects the geometry of the packing. The resulting horizontal force for the onset of motion is $T = \mu N$, now with

$$\mu = \tan(\alpha + \alpha_g), \tag{19}$$

α is the friction angle at the scale of contact. The geometrical contribution to the effective friction is fundamental as it explains the Coulomb-like behavior observed numerically for frictionless particles.

This provides the basic explanation for the angle of repose of a sand heap (Fig. 7a). The pile is stable as long as its slope is small enough to prevent gravity forces to reach this criterion. Above the threshold, an avalanche nucleates that flows down the pile (Douady et al., 1999; Quartier et al., 2000). In practice, the measurement of the avalanche slip-face angle with respect to the horizontal provides an easy and precise approximation of the effective friction coefficient. Typical values for aeolian sand are $\mu_s \simeq \tan(34°)$ and $\mu_d \simeq \tan(30°)$.

3.3.4. Collisions of two elastic particles

When two elastic spheres collide each other, their kinetic energy is converted into elastic energy in the vicinity of the contact. The collision time t_c scales as δ/v, where v is the normal impact velocity and δ the contact deformation (Fig. 5a). Hertz's law is still valid during the collision if the impact velocity v is much smaller than the propagation speed of elastic waves inside the grain, $c \propto \sqrt{E/\rho_p}$. Under this assumption

$$t_c \propto \frac{d}{c}\left(\frac{c}{v}\right)^{1/5}. \tag{20}$$

This collision time is typically on the order of a microsecond for sand grains.

3.3.5. Restitution coefficient

Real collisions are not perfectly elastic and the impact is eventually dissipative. The inelasticity coefficient, also called the energy restitution coefficient, is defined as

$$v' = -ev, \tag{21}$$

where v and v' are the velocities before and after the shock. e is always smaller than unity and depends on the material properties as well as on impact velocities. This physical energy loss can originate in various ways. For instance, in the case of plastic dissipation in the contact area, Johnson (1985) has derived the following scaling law

$$e \sim \left(\frac{H}{E}\right)^{1/2}\left(\frac{\rho_p v^2}{H}\right)^{-1/8} \propto v^{-1/4}, \tag{22}$$

which has been approximately verified for metallic beads at moderate impact velocities.

3.3.6. Viscous loss in the fluid

The fluid characteristics also affect collisions between particles. In the context of this aeolian review, the following considerations are important for addressing transport in other atmospheres (e.g. Mars, Venus or Titan). Gondret et al. (1999, 2002) have performed experiments in which spherical beads rebound on a planar solid inside fluids of different densities and viscosities. They have shown the existence of a transition between a regime in which the bead rebounds after the collision and a regime in which the bead remains glued on the plane. These experiments show that the dimensionless parameter controlling the transition is the Stokes number St, which characterizes the ratio of the grain inertia and the viscous force.

Fig. 8 shows that the measurements $e(\mathrm{St})$ collapse on a single curve. The restitution coefficient is null below a threshold Stokes number equal to several units. Above this threshold, it increases and tends to a constant at large St. An estimation of the Stokes number for Mars, Venus and Titan environments show that St is greater than several thousand in all these cases, i.e. in the asymptotic regime of the curve displayed in Fig. 8.

3.4. Discrete element numerical simulations for sand transport

Models and numerical simulations provide a useful tool to investigate the properties of aeolian transport. Various simulation techniques and basic equations have been introduced, and assumptions made. Based on the ideas of Owen (1964), Anderson and Hallet (1986), Anderson and Haff (1988, 1991), Werner (1990), McEwan and Willetts (1991, 1993), Rasmussen and Sorensen (2008), Kok and Renno (2009), and Creyssels et al. (2009) – among others – have solved a simplified hydrodynamic model that
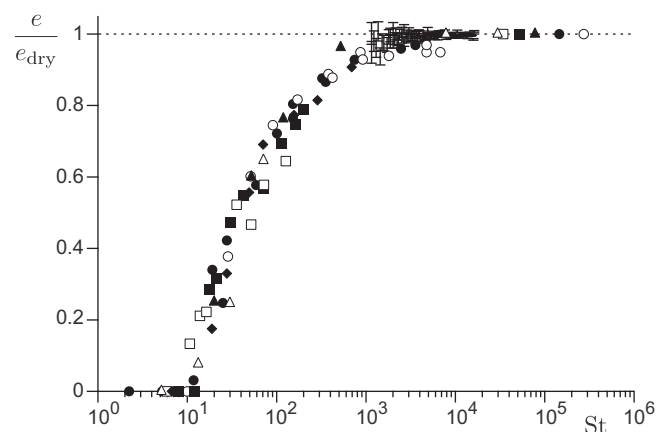

Fig. 8. Restitution coefficient e, normalized by its value e_{dry} measured without interstitial fluid, as a function of the Stokes number St. Beads and fluids of different natures are used (after Gondret et al. (2002)).

neglects the turbulent fluctuations (see Section 2). They have also approximated the interactions between the saltating grains and the bed by the so-called splash function, calibrated through single grain collision experiments or simulations performed in the absence of wind (Anderson and Haff, 1988; Rioual et al., 2000; Ammi et al., 2009), or dense saltation (McEwan et al., 1992). Alternatively, Almeida et al. (2008) recently modeled saltation considering more complete aerodynamic relationships and explicitly accounting for wind fluctuations. However, the splash process i.e. the ability of the grains in motion to expel other grains from the bed, was neglected. In particular, the balance between erosion and deposition was replaced by the maximization of the sediment flux with respect to the number of grains released per unit surface and unit time.

For this review, we have performed simulations based on discrete elements (so-called 'molecular dynamics' simulations). By contrast to previous approaches, it allows us to resolve simultaneously the motion of the grains and their interactions, taking the fluid flow into account. No splash function is therefore required. We follow all trajectories of typically several thousands of grains, solving Newton's law at each time step, which makes necessary calculation of all forces acting on the grains, as described in the previous sub-sections. In our simulations, grains in contact interact through elastic and frictional forces. A constant restitution coefficient is used when two grains collide – mid-air grain collisions (Sørensen and McEwan, 1996) are treated in the same way as those involving the grains on the bed. Forces exerted by the fluid on the grains are restricted to drag forces, with a drag coefficient function of the particle Reynolds number (see expression (17)). Solving the full fluid dynamics simultaneously to the grain motion is computationally too expensive. We have thus used the Reynolds averaged equations governing the mean flow properties, with a Prandtl-like mixing length approach for the turbulence closure. We account for the feed back of the grains on the fluid by a momentum balance (see Section 6.2). Finally, the equations governing the velocity $\vec{u}^p$ and the angular velocity $\vec{\omega}^p$ of a given particle p, whose mass is m^p, moment of inertia is I^p, and has N_p neighbors, are

$$m^p \partial_t \vec{u}^p = m^p \vec{g} + \sum_{c=1}^{N_p} \vec{f}^{pc} + \vec{F}_d^p, \tag{23}$$

$$I^p \partial_t \vec{\omega}^p = \sum_{c=1}^{N_p} \vec{r}^{pc} \times \vec{f}^{pc}. \tag{24}$$

$\vec{g}$ is the gravity acceleration vector, $\vec{f}^{pc}$ is the contact force at contact c, $\vec{r}^{pc}$ is the radius vector in the contact direction and $\vec{F}_d^p$ is the drag force.

The equations of motion coupled with the simplified fluid dynamics are then solved for spherical grains until a steady state is reached. Although the real grain shape is not actually spherical, this necessary simplification does not change the fundamental mechanisms behind sediment transport and with we are able to reproduce the aeolian transport phenomenology and related scaling laws. The result of our simulations is used in the following sections to complement the available experimental data.

4. Continuum description of aeolian transport

In this section, we present a framework describing erosion and transport in a unified way. We first define the interface that separates the granular bed from the fluid, and introduce the sediment fluxes that quantify mass exchange through and along it. We then consider steady homogeneous transport, which allows us to define the saturated flux. Finally, we propose a simple description of the saturation transient.

4.1. Interface between the sand bed and the fluid

One can think of two possible definitions of the interface separating the granular bed from the fluid. A first possibility is to introduce the surface ζ_s below which grains are static, and above which they move (Fig. 9a). Within a good approximation, the velocity of the wind vanishes at ζ_s. Another option is to consider the fictitious bed surface ζ one would obtain after all moving grains have been deposited on the bottom, forming a homogeneously packed bed (Fig. 9b). Describing the system in a continuous manner by the volume fraction ϕ, this interface reads

$$\zeta = \int_{-\infty}^{\infty} \frac{\phi}{\phi_b} dz, \tag{25}$$

where ϕ_b is the packing fraction of the bed. In the context of aeolian transport, the difference between ζ and ζ_s is small. We shall then assume in the rest of the paper that they coincide.

4.2. Flux and mass conservation

Particle transportation can be quantified by two different fluxes. The first type, denoted by q, counts the grains that cross, per unit time, a surface of unit width transverse to the transport direction, which extends from the bed to infinity (Fig. 10a). Defining the mean particle velocity $\langle \vec{u}^p \rangle$, we can write

$$\vec{q} = \int \frac{\phi}{\phi_b} \langle \vec{u}^p \rangle dz. \tag{26}$$

Note that with this definition, q is a *volumetric* flux i.e. a volume of grains (at the bed packing fraction) per unit time and unit length. Its dimension is that of a diffusion coefficient (m²/s). One can equivalently define a *mass* flux $\vec{q}_m = \rho_p \phi_b \vec{q}$. Using the effective interface ζ and the flux q, the mass conservation equation – the so-called Exner equation – then reads

$$\frac{\partial \zeta}{\partial t} = -\vec{\nabla} \cdot \vec{q}. \tag{27}$$

By contrast, the ascending flux $\varphi_\uparrow$ (resp. descending flux $\varphi_\downarrow$) counts the volume of grains (again at the bed packing fraction) that crosses a unit horizontal surface from below (resp. from above), see Fig. 10b. These *volumetric* fluxes have the dimension of velocity (m/s). The balance between erosion and deposition, which governs the bed evolution, reads

$$\frac{\partial \zeta_s}{\partial t} = \varphi_\downarrow - \varphi_\uparrow. \tag{28}$$

The difference $\varphi_\downarrow - \varphi_\uparrow$ is then the velocity of the bed surface.
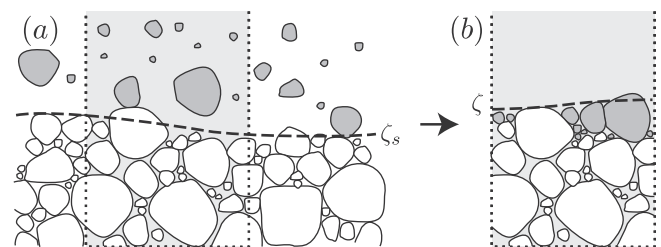

Fig. 9. The two definitions of the interface between the granular bed and the fluid. (a) Interface ζ_s between moving and static grains. (b) Effective interface ζ, defined after all moving grains are (virtually) deposited on the bed, at the same packing fraction ϕ_b.
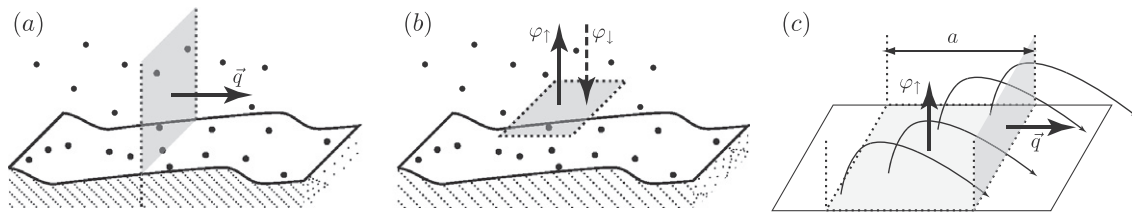
Fig. 10. Schematics for (a) the horizontal flux $\vec{q}$ and (b) the ascending $\varphi_\uparrow$ and descending $\varphi_\downarrow$ vertical fluxes. (c) In steady homogeneous state, vertical fluxes are equal $\varphi_\uparrow = \varphi_\downarrow = \varphi$. Considering a single type of trajectory of hop length a, the horizontal and vertical fluxes are related to each other by $q = a\varphi$.

4.3. Saturated flux

Let us consider an infinite flat granular bed subjected to a homogeneous turbulent wind in a statistically steady state. The transport and flow eventually reach an equilibrium state due to the negative feed back of the grains on the flow, which is characterized by the so-called saturated flux $q = q_{sat}$. 'Equilibrium' is used here to infer a 'steady homogeneous state' differing from the thermodynamical definition, where the saturated state is out of equilibrium, because energy is being injected continuously by the wind in the transport layer. As the sand flux is spatially homogeneous, there is no net erosion nor deposition of grains: $\varphi = \varphi_\downarrow = \varphi_\uparrow$. As pointed out by Jensen and Sørensen (1982, 1986), the ratio q_{sat}/φ can be interpreted as the mean hop length (Fig. 10c). As discussed in Section 2, the saturated flux q_{sat} is a function of the shear velocity u_* defined at the proper time and length scales.

The transport law $q_{sat}(u_*)$ must usually be calibrated experimentally. For example, in the field, this can be achieved by using dunes or superimposed undulations as perfect sand traps, while the wind velocity must be measured close to the bed. In a wind tunnel, this is achieved through the challenging task of obtaining both a homogeneous flow and a saturated transport, and measuring the sand flux (White and Mounla, 1991). For this, vertical samplers are normally used, designed to minimize the disturbances of the trap on the wind (Zingg, 1953; Goosens et al., 2000). Using such samplers, one needs to pay attention to the fact that most transport takes place within the first two centimeters above the ground. Besides, as demonstrated in Rasmussen and Mikkelsen (1991), vertical samplers can underestimate the total flux, due to erosion under the trap and to the passage of ripples. An alternative to sand traps is to measure the erosion rate along the axis of the wind tunnel and to integrate it in space to get the flux.

There has been a great effort to obtain experimentally (Chepil and Milne, 1939; Bagnold, 1941; Zingg, 1953; Williams, 1964; Svasek and Terwindt, 1974; Nickling, 1978; White, 1979; Jones and Willetts, 1979; Willetts et al., 1982; Rasmussen and Mikkelsen, 1991; Greeley et al., 1996) using both wind tunnels and atmospheric flows in the field to determine the relationship between the saturated flux over a flat sand bed and the shear velocity u_*. The transport law $q_{sat}(u_*)$ presents very robust features, as exemplified in Fig. 11. The saturated flux is an increasing function of the shear velocity u_*, it vanishes below a threshold shear velocity u_d and it decreases with the grain diameter. It is difficult to go beyond these basic observations on the basis of experimental relations $q_{sat}(u_*)$ only. Most models effectively provide an equally good fit of the data and there is a huge dispersion of measurements in the literature. One of the most complete wind tunnel measurements were performed by Iversen and Rasmussen (1999) using sand of different sizes (in the range 100–600 μm) and a large range of shear velocities (up to 1 m/s or about five times u_{th}). As shown in Andreotti (2004) and Durán and Herrmann (2006), the proper way to test the scaling behavior from this data is to rescale the flux and to plot q_{sat}/u_*^2 as a function of u_* (Fig. 12). Depending on the series
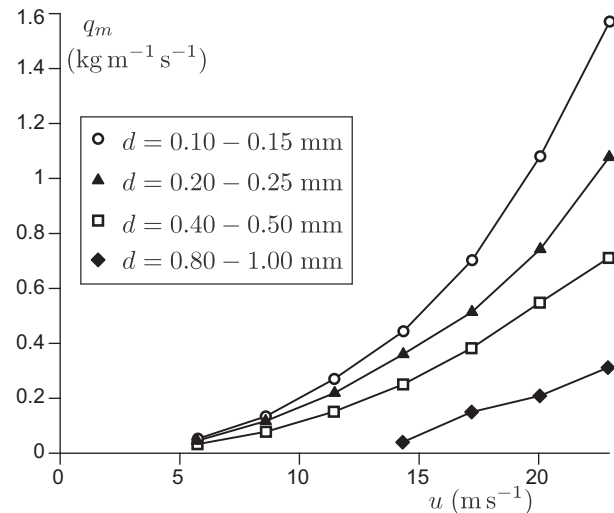

Fig. 11. Wind tunnel measurements of the mass flux as function of the wind velocity at the center of the tunnel for different grain sizes. Data from Dong et al. (2003).

of data, q_{sat}/u_*^2 is observed to increase or decrease with u_* for large winds. No systematic trend with the grain diameter was observed once the flux was rescaled. In the first approximation, one can therefore conclude from Iversen and Rasmussen (1999) that the saturated flux scales as $q_{sat} \propto u_*^2 - u_d^2$. The same behavior is also found in wind tunnel experiments by Creyssels et al. (2009), exploring shear velocities up to three times the threshold value u_d. Interestingly, Ho et al. (2011) have shown that, for the same experimental conditions as those of Creyssels et al. (2009), the sand flux is proportional to u_*^3 in the case of saltation over a rigid non erodible bed.

Numerical simulations (Werner, 1990; Andreotti, 2004; Almeida et al., 2008; Kok and Renno, 2009; Creyssels et al., 2009 and ours) provide a useful complement for the calibration of the saturated flux in the absence of shear stress fluctuations. They show that the saturated flux varies linearly with u_*^2 for shear velocities up to four times u_d (see Fig. 13 for a typical example). However, for shear velocities well above the threshold – say, above $5u_d$, which is a condition difficult to achieve in a wind tunnel – we have found that the saturated flux starts to scale as u_*^3 (Fig. 13).

4.4. Saturation length

We consider now a situation for which the flow is not homogeneous in space or time, e.g. the wind over an undulating topography. The saturation process described above does not occur instantaneously: the flux q follows the saturated flux corresponding to the local basal shear stress, with a space lag (Bagnold, 1941; Sauermann et al., 2001) or a time lag (Anderson and Haff, 1988, 1991). One can account for this delay by a first order
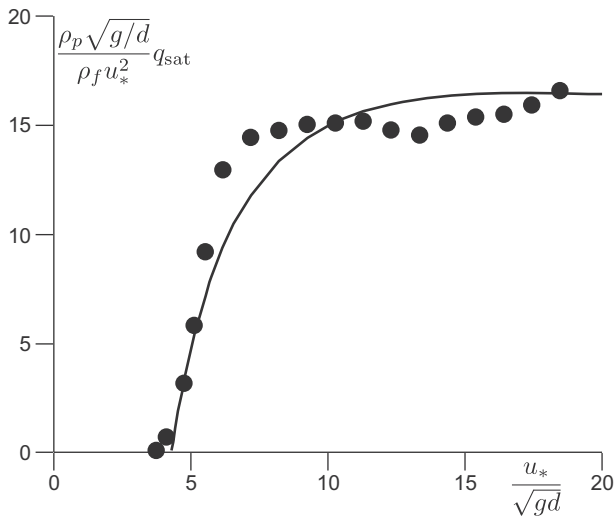
Fig. 12. Wind tunnel measurement of the dimensionless saturated flux (Iversen and Rasmussen, 1999) for $d = 242$ μm. The flux is normalized by u_*^2 in order to show the asymptotic behavior. The solid curve corresponds to a flux proportional to $u_*^2 - u_d^2$.
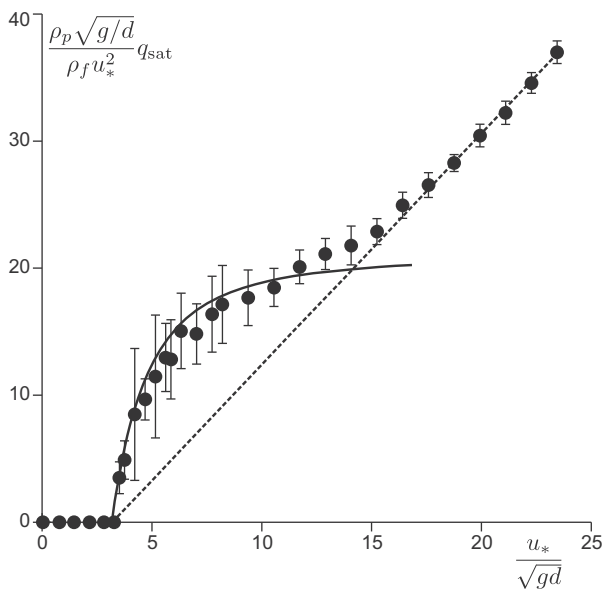

Fig. 13. Dimensionless saturated flux obtained from our numerical simulations of aeolian transport. Note the two asymptotic behaviors of the saturated flux: proportional to $u_*^2 - u_d^2$ close to the threshold (solid line) and to u_*^3 well above it (dashed line).

relaxation differential equation (Andreotti et al., 2002a,b), which results from the linearization around the saturated state:

$$T_{sat} \frac{\partial q}{\partial t} + L_{sat} \frac{\partial q}{\partial x} = q_{sat} - q, \tag{29}$$

where T_{sat} and L_{sat} are the saturation time and length.

These two quantities can be considered separately in two pure situations. The first one is that of a uniform flat sand bed subjected to a sudden change in wind velocity. The flux is then homogeneous in space, but relaxes in time towards the new saturated flux q_{sat} after the change. The second situation consists of a steady wind over a sand bed which extends in the half-space $x > 0$ only. The upstream ($x < 0$) region is non erodible, but of same hydrodynamical roughness. The sand flux is null at the bed entrance ($x = 0$). It

increases further downstream, and eventually relaxes exponentially towards q_{sat} over a characteristic length L_{sat}. Measurements of the saturation length based on this experimental geometry are presented in Section 5.2.

The saturation time T_{sat} is generally much smaller than the typical evolution time scale of the bed, so that, as far as geomorphology problems are concerned, it can be neglected. Hydrodynamics and sediment transport can thus considered and treated as if the bed was fixed. Finally, this formalism emphasizes the fact that neither the flux q nor the erosion rate $\partial_t h$ are functions of the shear velocity u_*. Regardless of the wind velocity magnitude, if q is above q_{sat} it must decrease, leading to sand deposition, while, if q is below q_{sat} it must increase, leading to erosion of the sand bed. Below the transport threshold, the saturated flux is null so that deposition must occur. However, above the threshold, erosion or deposition takes place depending on the gradient of u_*.

The description of the saturation transient by a first order relaxation equation has been successfully applied to the description of dune formation by Andreotti et al. (2002b), Elbelrhiti et al. (2005), Valance and Langlois (2005), Charru (2006), Claudin and Andreotti (2006), and Fourrière et al. (2010). Fig. 14 shows a visual interpretation of the saturation length in that case. Due to aerodynamic effects, the maximum of the basal shear stress is located upwind of the crest of a small proto-dune, at a distance proportional to the wavelength. The saturated flux thus presents a maximum at the same place. However, the maximum of the actual sand flux q is reached at a distance L_{sat} downwind of this point. Finally, the evolution of the bump depends on the position of the flux maximum with respect to the crest. In Fig. 14, the crest is located in the deposition zone so that the proto-dune grows.

In three dimensions, the sand flux is not a scalar but a two components vector $\vec{q} = (q_x, q_y)$. The saturated flux is then aligned with the basal shear stress $\vec{\tau} = \rho_f u_*^2 \vec{e}_\parallel$ ($e_\parallel$ is the unit vector parallel to the shear stress). The saturation equation can then be generalized as

$$T_{sat} \frac{\partial \vec{q}}{\partial t} + L_{sat} \left(\vec{e}_\parallel \cdot \vec{\nabla} \right) \vec{q} = q_{sat} \vec{e}_\parallel - \vec{q}, \tag{30}$$

which traduces the fact that both the flux and the direction of transport are lagged.

5. Static and dynamic thresholds

A fluid flow can only entrain grains from a sand bed when the velocity exceeds a threshold. In this section, we introduce the Shields number, which is the dimensionless number traditionally used to describe the onset of transport. We also describe the influence of the bed slope and cohesion on this threshold. The static threshold, which originates from the direct entrainment of the grains by the fluid, must not be confused with the dynamic
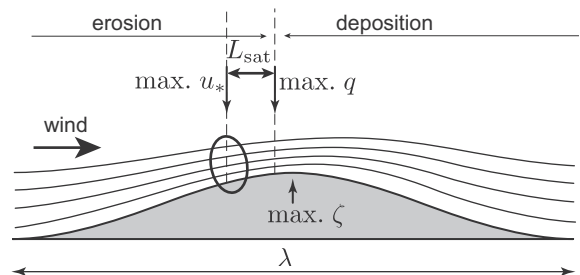

Fig. 14. Schematic of the streamlines above a low amplitude undulation on the surface of the sand bed. The maximum shear velocity is located at a distance upwind from the crest (maximum of ζ) proportional to the wavelength λ. The sand flux maximum is located at a distance L_{sat} downwind. It separates the erosion zone from the deposition zone.

threshold, above which saltation can be sustained by the impacts of the grains on the bed. The latter is specific to an aeolian situation, while the physics of the static threshold is the same in any fluid (air and water specifically). The dynamic threshold is typically lower than the static one and is thus more relevant in aeolian transport. Nevertheless, the concepts introduced in this section, as well as the scaling laws regarding slope and cohesion effects, are useful for the understanding and the description of aeolian transport.

5.1. The Shields number

Let us consider a spherical grain trapped in the hole between its two fixed neighbors (Fig. 15b). This grain is subjected to a drag force F_d from the flow above it. We assume for the moment that cohesion is negligible, so that contact friction is the only interaction between the grains. The considered grain looses static equilibrium when F_d balances weight minus buoyancy $P \sim \pi/6(\rho_p - \rho_f)$

Fig. 15. (a) Static and dynamic threshold Shields numbers Θ_s and Θ_d as a function of the grain size d rescaled by the viscous diameter $d_v = (\rho_p/\rho_f - 1)^{-1/3}\nu^{2/3}g^{-1/3}$. White symbols (○) correspond to the static threshold, obtained from subaqueous measurements by Fernandez Luque and van Beek (1976) and collected by Yalin and Karahan (1979). Black symbols (■) correspond to the dynamic threshold obtained from aeolian measurements performed by Chepil (1945a,b,c) and Hsu (1971). Inset: schematics showing the mechanical origin of the transport threshold at the grain scale. (b) Dynamic threshold shear velocity as a function of the grain diameter for aeolian transport. Measurements performed by Chepil (1945a,b,c) and Hsu (1971) (○) and by Rasmussen et al. (1996) (□). Solid and dotted lines show the predictions of the model developed here, when cohesion is taken into account.

gd^3, times the effective friction coefficient μ discussed in Section 3.3.3. The quantitative criterion for onset of motion is then the ratio $F_d/(\rho_p - \rho_f)gd^3$.

In order to obtain the threshold value of this ratio, it is necessary to relate the drag force to the aerodynamic control parameters. From a dimensional analysis, the force exerted by the fluid on a flat surface of the size of a grain is proportional to τd^2, where τ is the shear stress at the fluid/grain interface. The relevant dimensionless number is then the so-called Shields number defined as

$$\Theta = \frac{\tau}{(\rho_p - \rho_f)gd} = \frac{\rho_f u_*^2}{(\rho_p - \rho_f)gd}. \tag{31}$$

This suggests that the onset of grain motion is controlled by a threshold Shields number $\Theta_s \propto \mu$, i.e. independent of the grain size, as well as the density and the nature of the fluid. In Fig. 15a, we show this Shields number as a function of the grain size for fluids of different viscosities, in laminar and turbulent flow regimes. One can see that Θ_s is fairly constant for large grains but gets larger for smaller d. Moreover, the value of the threshold Shields number is 10 times smaller than the effective friction coefficient μ. This means that the grains that move first receive 10 times more momentum per unit time than an average grain of the surface. In other words, when motion starts, only a small fraction of grains at the surface get entrained. This suggests that the relation between the drag force F_d exerted on those grains and the basal shear stress τ is not straightforward.

The problem may be solved using dimensional analysis. One first assumes that the grains are sufficiently large not to be sensitive to cohesion. The fluid to grain density ratio only appears in front of gravity. Thus, using the fluid kinematic viscosity ν, a single characteristic length-scale can be built: the viscous diameter:

$$d_v = \left(\frac{\rho_p}{\rho_f} - 1\right)^{-1/3} \nu^{2/3} g^{-1/3}, \tag{32}$$

which corresponds to the grain size for which inertia, gravity and viscosity are of the same order of magnitude. The threshold Shields number should thus depend on the ratio d/d_v, only. Fig. 15 shows that experimental values of the threshold obtained in liquids of different viscosities collapse on a master curve $\Theta_s(d/d_v)$. However, the threshold Shields number for aeolian transport is much smaller, which points to a different origin. Aeolian transport can be sustained even below the minimal wind for which grains can be entrained.

5.2. Static threshold

Before modeling this dynamic threshold, let us discuss further the static one. We will focus on the grain configuration shown in Fig. 15, aiming to relate $\vec{F}_d$ to τ, and to understand the shape of the relation $\Theta_s(d/d_v)$.

5.2.1. Viscous regime

In a Newtonian fluid at small Reynolds number, the viscous stress reads: $\tau = \eta \partial u_x/\partial z$. Assuming that the velocity profile is linear close to the sand bed ($u_x = (\tau/\eta)z$), the effective flow velocity u around the grain can be approximated by that at the height $z = d/2$:

$$u \sim \frac{\tau d}{2\eta}. \tag{33}$$

One can roughly estimate that only the upper part of the grain is submitted to the viscous stress. The resulting drag force is equal to $F_d \sim (3/2)\pi\eta du$, which can also be written as $F_d \sim (3\pi/4)\tau d^2$ according to (33). At the threshold, this force balances friction exactly
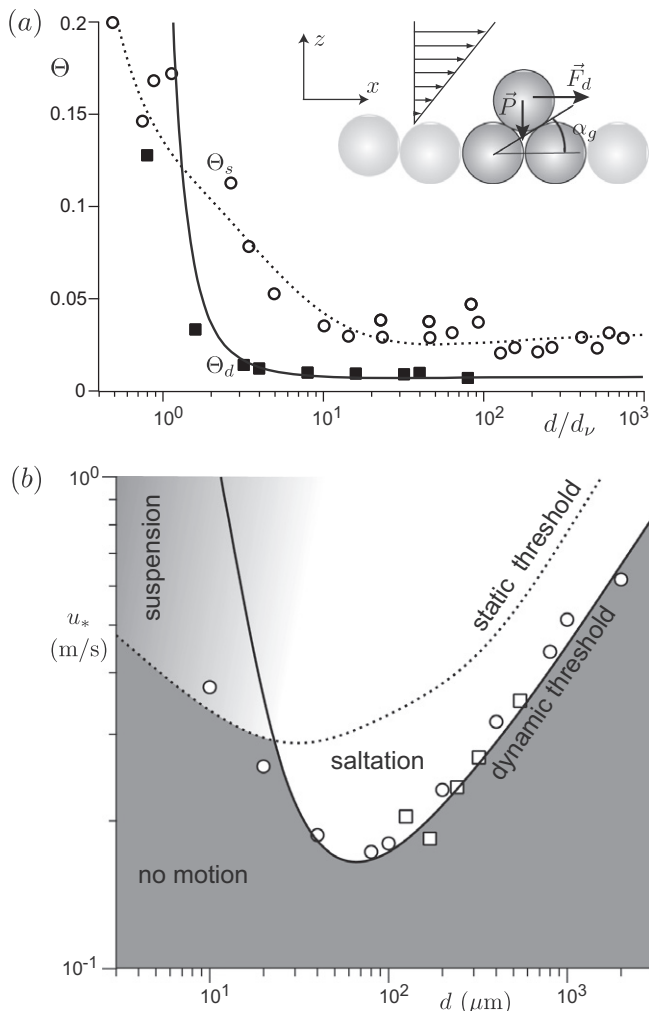
$$\frac{\pi}{6}\mu(\rho_p - \rho_f)gd^3 \sim \frac{3\pi}{4}\tau_s d^2, \tag{34}$$

where τ_s is the threshold shear stress. This relation predicts a threshold Shields number constant and equal to

$$\Theta_s \sim \frac{2}{9}\mu. \tag{35}$$

This estimate leads to a threshold Shields number around 0.14 for rough grains, which is consistent with experimental data.

5.2.2. Turbulent regime

In the turbulent limit, the velocity profile above the sand bed is logarithmic and one still assumes that the flow velocity around the grain is the fluid velocity at $z = d/2$. For simplicity, we only consider a turbulent drag force on the upper part of the grain so that the equilibrium now reads:

$$\frac{\pi}{6}\mu(\rho_p - \rho_f)gd^3 \sim \frac{\pi}{16}C_\infty\rho_f(u_s)^2 d^2 \sim \frac{\pi C_\infty}{16\kappa^2}\ln^2\left(\frac{d}{2z_0}\right)\tau_s d^2, \tag{36}$$

where μ is the effective friction coefficient and u_d the fluid velocity at the threshold. The threshold Shields number is thus constant in the turbulent regime and equal to

$$\Theta_s = \frac{8\mu\kappa^2}{3C_\infty\ln^2(d/(2z_0))}. \tag{37}$$

The typical value $\simeq 0.04$ measured in liquids can be recovered with a typical roughness $z_0 \simeq d/30$ and a drag coefficient $C_\infty = 1/2$ (for spheres).

5.2.3. Crossover between the viscous and turbulent regimes

It is interesting to establish an expression valid in both the viscous and turbulent regimes. We introduce the rescaled velocity around the grain as

$$S = \frac{\rho_f u^2}{(\rho_p - \rho_f)gd}. \tag{38}$$

As discussed in Section 3.1, the drag force can be written under the form $\frac{\pi}{16}d^2 C_d \rho_f U^2$, where the drag coefficient $C_d = [C_\infty^{1/2} + s\mathcal{R}^{-1/2}]^2$ depends on the grain-based Reynolds number $\mathcal{R} = Ud/\nu$. For natural sand grains, the constants are $C_\infty \simeq 1$ and $s \simeq 5$ (Ferguson and Church, 2004). From these expressions, one gets the equation on the rescaled velocity, S_f

$$(C_\infty S_s)^{1/2} + s\left(\frac{d_v}{d}\right)^{3/4}S_s^{1/4} = \left(\frac{8\mu}{3}\right)^{1/2}, \tag{39}$$

which solves into

$$S_s = \frac{1}{16C_\infty^2}\left[\left(s^2\left(\frac{d_v}{d}\right)^{3/2} + 8\left(\frac{2\mu C_\infty}{3}\right)^{1/2}\right)^{1/2} - s\left(\frac{d_v}{d}\right)^{3/4}\right]^4. \tag{40}$$

To get the critical Shields number, one has to link S_s to the fluid stress. For this, one assumes that the viscous stress and the Reynolds stress can be added

$$\tau = \frac{2\eta}{d}u + \frac{\rho_f\kappa^2}{\ln^2(d/(2z_0))}u^2. \tag{41}$$

One obtains the threshold Shields number

$$\Theta_s = 2\left(\frac{d_v}{d}\right)^{3/2}S_s^{1/2} + \frac{\kappa^2}{\ln^2(d/(2z_0))}S_s. \tag{42}$$

Fig. 15 shows the comparison of this model with experimental data obtained in liquids. Note that measurements of the static threshold performed in the air (Willetts et al., 1991) are in fact very close to the dynamic threshold discussed below. The agreement is good in comparison to the simplicity of the description. In particular, it explains the drop of the Shields number by a factor of five between the viscous and the turbulent regimes. The drag force is more efficient in the turbulent regime than in the Stokes regime. Moreover, for a given stress, the fluid velocity around the surface grains is larger in the turbulent than in the viscous regime. The transition from one regime to the other occurs for grains of diameters $d \sim s^{4/3}(2\mu C_\infty)^{-1/3}d_v \simeq 200\ \mu m$. So, most of aeolian grains are precisely in the transition zone between viscous and turbulent regimes.

5.3. Dynamic threshold

We have seen that the static transport threshold is rarely observed in aeolian transport. Even below this threshold, transport can occur and reach a statistical steady state. As there are both turbulent fluctuations and disorder at the surface of the bed, the emphasis should not be understanding the initiation of transport but instead examining the minimal wind for which a non-zero flux can be sustained. This second threshold is called the dynamic threshold. To measure it in practice, one extrapolates to zero the curve relating the sediment flux to the shear velocity. It is thus defined in a much more precise way than the static threshold, for which a somewhat arbitrary criterion for the onset of particle motion has to be chosen.

The key aspect of aeolian transport explaining this dynamic threshold is the ability of grains in saltation to eject other grains. This process, called splash, is a statistical process, with a wide distribution of velocities and angles. If transport is in a steady state, the distribution of grain velocities is stationary with respect to the splash process. On average, each saltating grain produces a single saltating grain during a collision with the bed, either by rebound or by ejection. Of course, in this average, the fact that low energy grains have a high probability to stop is balanced by the increased role of ejection of new grains by high energy impacts. One can formally define the replacement capacity as the average number of saltating grains produced per collision. If the replacement capacity is larger than 1, the bed is eroded; if it is smaller than 1, there is deposition of sand. At saturation, the replacement capacity is exactly 1.

At equilibrium, the fluid shear stress is below the static threshold. The grains at the surface are thus trapped by a force larger than the hydrodynamic drag. The resistive force to overcome is equal to:

$$\frac{\pi}{6}\mu(\rho_p - \rho_f)gd^3\left(1 - \frac{\Theta}{\Theta_s}\right). \tag{43}$$

The replacement capacity of an impacting grain of velocity u^p is determined by its kinetic energy compared to the work of this resistive force over a displacement d. The non-dimensional number controlling the replacement capacity is thus:

$$\frac{\rho_p(u^p)^2}{(\rho_p - \rho_f)gd\left(1 - \frac{\Theta}{\Theta_s}\right)}. \tag{44}$$

As the particle velocities u^p scales on the wind shear velocity u_*, one infers that the overall replacement capacity is unity for a dynamic Shields number Θ_d given by

$$\Theta_d = b\frac{\rho_f}{\rho_p}\left(1 - \frac{\Theta_d}{\Theta_s}\right), \tag{45}$$

where b is a numerical constant. Inverting the relation, one gets:

$$\Theta_d = \frac{\Theta_s}{1 + \frac{\rho_p}{a\rho_f}\Theta_s}. \tag{46}$$

As a consequence, for a small density ratio ρ_p/ρ_f, the dynamic threshold is almost equal to the static threshold. Conversely, in

the limit of infinite density ratio (aeolian case), the dynamic threshold is much smaller than the static threshold ($\Theta_d \rightarrow b\rho_f/\rho_p$).

5.4. Influence of the bed slope

We now consider a sand bed with a slope $\tan\alpha$ in the direction of the flow (Fig. 16a). If this slope is upward, a stronger flow is required to move the grains. Conversely, the threshold is lower if the slope is downward (Fernandez Luque and van Beek, 1976; Iversen and Rasmussen, 1994; Rasmussen et al., 1996). In this case, the tangential force on a grain is modified as $F_d - P\sin\alpha$, while the normal force is $P\cos\alpha$. As a consequence the static threshold is reached when $F_d - P\sin\alpha = \mu P\cos\alpha$. This condition is written as

$$\Theta_s(\alpha) = \Theta_s(0)\left(\cos\alpha + \frac{\sin\alpha}{\mu}\right). \tag{47}$$

For the dynamic threshold Θ_d, one can follow the same reasoning from the previous section. An inclined bed modifies the non-dimensional number controlling the replacement capacity (Eq. (44)) as

$$\frac{\rho_p(u^p)^2}{(\rho_p - \rho_f)g\left(\cos\alpha + \frac{\sin\alpha}{\mu}\right)d\left(1 - \frac{\Theta}{\Theta_s(\alpha)}\right)}. \tag{48}$$

The slope modifies the particle velocity by a small factor proportional to the ratio of the particle vertical and the horizontal velocity times $\sin\alpha$. As this ratio is very small in saltation, the particle velocity is only weakly affected by the slope. This leads to the modify dynamic threshold

$$\Theta_d(\alpha) = \Theta_d(0)\left(\cos\alpha + \frac{\sin\alpha}{\mu}\right). \tag{49}$$

As expected, the bed slope has the same influence in both static and dynamic thresholds. This relationship is fairly well verified. This effect is however a bit weaker than expected, with a friction coefficient slightly larger than the avalanche slope (Fig. 16b).

5.5. Influence of cohesion

The threshold is larger in the presence of an additional cohesive force between the grains. Cohesion is more important for smaller grains. A realistic computation of cohesion can be achieved under the assumption that contacts between grains are made of many micro-asperities (Fig. 6). Whether these micro-contacts are in an elastic or plastic state, the scaling and transport threshold laws are essentially the same, and can be expressed as:
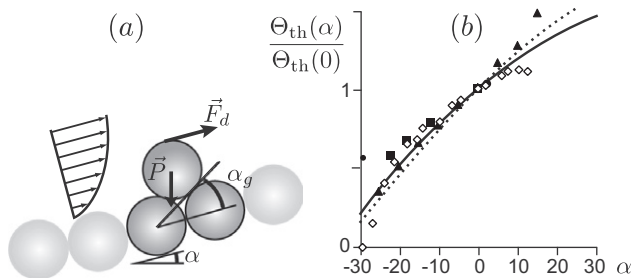

Fig. 16. (a) Schematics for the dependence of the threshold Shields numbers Θ_s and Θ_d on the bed slope α. (b) Variation of the threshold with the bed angle α. Black symbols correspond to the static threshold, obtained from subaqueous measurements by Fernandez Luque and van Beek (1976) (■) and Dey (2003) (▲) with natural sand grains. White symbols (◇) correspond to the dynamic threshold obtained from aeolian measurements performed by Hardisty and Whitehouse (1988). Solid line: proposed model. Dotted line: approximate expression $\cos\alpha + \sin\alpha/\mu$, with $\mu = \tan 35°$.

$$\Theta_{th} = \Theta_{th}^{\infty}\left[1 + \frac{3}{2}\left(\frac{d_m}{d}\right)^{5/3}\right], \tag{50}$$

with $d_m \propto (\gamma/M)^{3/5}[E/(\rho_s g)]^{2/5}$, where E is the grain Young modulus and where M is the grain hardness (or $M = E$ if the contacts are not plastified), and γ is the surface tension of the material they are made of, cf. Claudin and Andreotti (2006). This cohesive term is responsible for increasing the threshold at small d (Fig. 15a).

6. Saturated transport

Following the seminal work of Bagnold (1941), several attempts to model the steady or saturated transport from fundamental principles have been proposed (Kawamura, 1951; Owen, 1964; Kind, 1976; Lettau and Lettau, 1978; Jensen and Sørensen, 1986; Ungar and Haff, 1987; Anderson and Haff, 1988; McEwan and Willetts, 1993; Spies and McEwan, 2000; Sauermann et al., 2001; Sørensen, 2004; Andreotti, 2004; Creyssels et al., 2009). An important objective of these works is to provide a macroscopic transport law relating the saturated flux to the shear velocity based on microscopic and empirical inputs. In this section, we also aim to provide scaling laws, not only for the saturated flux, but also for other quantities like the transport roughness and the particle volume fraction. We show how to develop a consistent description of sand transport from the properties of the fluid and the particles within and above the transport layer. Interestingly, we evidence a crossover from a low-velocity regime (typically for $u_*/u_d < 4$) where q_{sat} scales like u_*^2 as predicted in the model of Ungar and Haff (1987), to a high-velocity Bagnold-like regime, where $q_{sat} \propto u_*^3$.

6.1. Negative feedback of particles on the flow

6.1.1. Qualitative description

Steady transport of sand by wind flow is the result of several processes. The grains in motion are accelerated by the drag force exerted by the flow. When the moving grains collide with the bed, they may rebound and/or eject other particles (splash), which, due to irregularities on the surface, can jump high enough to feel the wind and be themselves accelerated (Fig. 17a). These grains in motion form a transport layer, whose thickness is related to the hop height of the grains, see the visualization of grain trajectories in Fig. 17b. This transfer of momentum from the flow to the grains results in a negative feedback on the wind velocity, which is reduced in the transport layer.

As discussed above for the dynamic threshold (Section 5.3), the condition for a steady transport is that the replacement capacity is exactly one. In mechanical terms, this means that saturation corresponds to the point where the negative feedback of transport on the flow has reduced the wind shear velocity to the dynamical threshold u_d. We present below two pieces of evidence of such a feedback.

6.1.2. Particle density profile

In the saturated state, aeolian transport is characterized by a diffuse layer above the bed. This layer can be seen in Fig. 17, that visualizes the typical trajectory of particles flying above aeolian ripples. Quantitatively, the distribution of grains in this layer has been measured for different wind intensities (White, 1982; Namikas, 2003; Liu and Dong, 2004; Rasmussen and Sorensen, 2008; Creyssels et al., 2009). The vertical profiles of the volume fraction $\phi(z)$ decreases exponentially with altitude (Fig. 18), which corresponds to a maxwellian (i.e. Gaussian) distribution of vertical velocities out of the bed. This supports the gas picture for the grains in the transport layer.
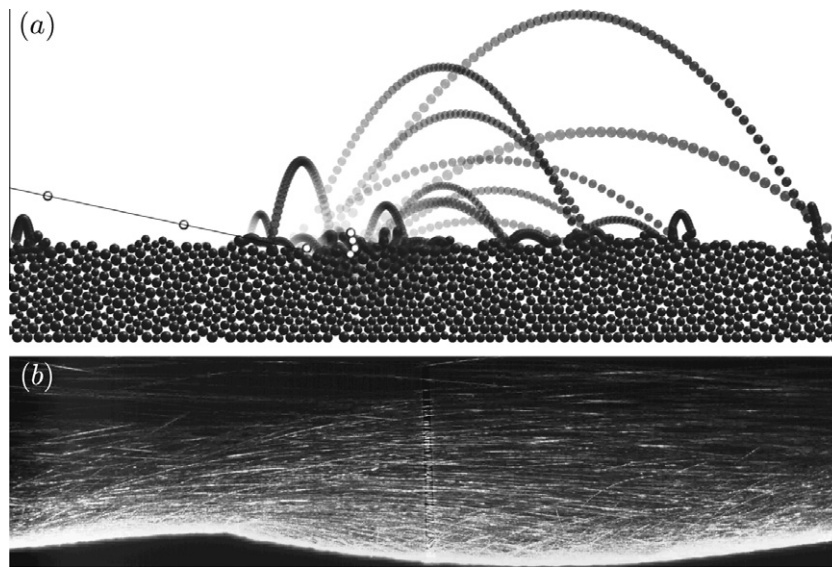
Fig. 17. (a) Grains ejected after a high energy collision (numerical simulations). (b) Visualization of the trajectories of the grains flying over aeolian ripples.

Importantly, these measurements show that the characteristic height over which the volume fraction decreases, which is a measure of the typical height of the transport layer, is independent of the wind shear velocity over the measured range (Fig. 18). Jensen and Sørensen (1986) also found that the probability distribution of the jump height does not depend on the wind shear velocity (over the experimental range). Therefore, the mechanism responsible for the saturation of the transport inside this transport layer, close to the bed, should also be independent of the wind shear velocity. This is direct evidence of the negative feedback induced by sediment transport on the flow. In contrast, Ho et al. (2011) have provided experimental evidence that in the case of saltation over a rigid (i.e. non erodible) bed, the thickness of the transport layer is much larger (several tens of centimeters) and varies significantly with u_*, meaning that in this much more dilute situation, there is almost no feed back of the moving grains on the flow.

6.1.3. Aerodynamic roughness length

Another direct indication of the negative feedback of grains on the flow comes from measurements of the aerodynamic roughness z_s above the transport layer. In the presence of sediment transport, the roughness length of the logarithmic wind velocity profile far above the bed is not related to the geometrical roughness (of the order of the grain diameter d), nor to the size of the viscous sub-layer
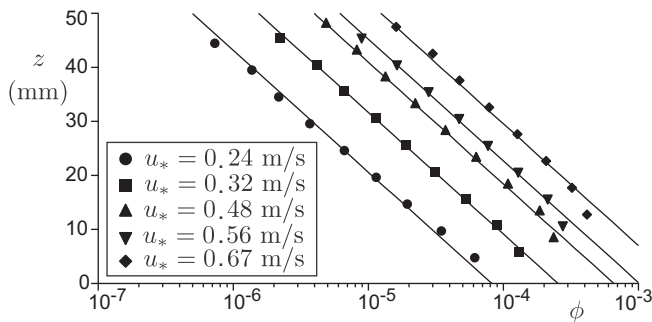

Fig. 18. Wind tunnel measurements of the vertical profiles of the volume fraction ϕ (z) of the grains in saltation for different shear velocities u_*. In the explored range of shear velocities the volume fraction decreases exponentially with a characteristic height of about 10 mm, independently of the shear velocity. Data from Creyssels et al. (2009).

(proportional to $\sim v/u_*$). Instead, it depends on the details of the saltation process, in particular, grain trajectories and vertical distributions. This is the picture suggested by the experimental findings (see Fig. 19) that shows a consistent increase of the aerodynamic roughness with the wind shear velocity (Sherman, 1992; Sherman and Farrell, 2008). The apparent increment of the surface roughness is due to the larger amount of momentum extracted from the flow by the sediment transport, which effectively leads to an upward shift of the height at which the wind velocity tends to zero.

6.2. Shear stress partition

Following the ideas Owen (1964), one can divide the overall shear stress, which is the flux of horizontal momentum through a horizontal surface, into two contributions: the momentum flux due to the fluid turbulent fluctuations and the momentum flux carried by the particles. In a steady homogeneous state, the shear stress should not depend on height. In other words, the momentum flux is conserved. We consider average grain trajectories taking off the bed with a velocity $\langle u_\uparrow^p \rangle$, and coming back to it with $\langle u_\downarrow^p \rangle$ after a hop of length a. This balance can be written as

$$\tau \equiv \rho_f u_*^2 = \tau_b + \rho_p \phi_b \varphi \left(\left\langle u_\downarrow^p \right\rangle - \left\langle u_\uparrow^p \right\rangle \right)$$

$$= \tau_b + \rho_p \phi_b \frac{\left(\langle u_\downarrow^p \rangle - \langle u_\uparrow^p \rangle \right)}{a} q. \tag{51}$$

This formula can also be found (with different notation) in Sørensen (2004). The left hand side term is the shear stress applied far above the bed, i.e. in the region where the flow is undisturbed by the presence of transport. It must equal the sum of the basal shear stress and the momentum flux due to ascending and descending grains. At saturation, erosion balances deposition so that the replacement capacity is equal to one. As a consequence, the basal shear stress reaches it threshold value $\tau_d = \rho_f u_d^2$, so that one can write the saturated flux as

$$q_{\text{sat}} = \frac{\rho_f (u_*^2 - u_d^2) a}{\rho_p \phi_b \left(\left\langle u_\downarrow^p \right\rangle - \left\langle u_\uparrow^p \right\rangle \right)} \tag{52}$$

(Sørensen, 2004). In order to go beyond this expression, one needs to estimate the hop length a and the velocities $u_\downarrow^p$ and $u_\uparrow^p$, i.e. to explore the properties of transport at the scale of the grain.
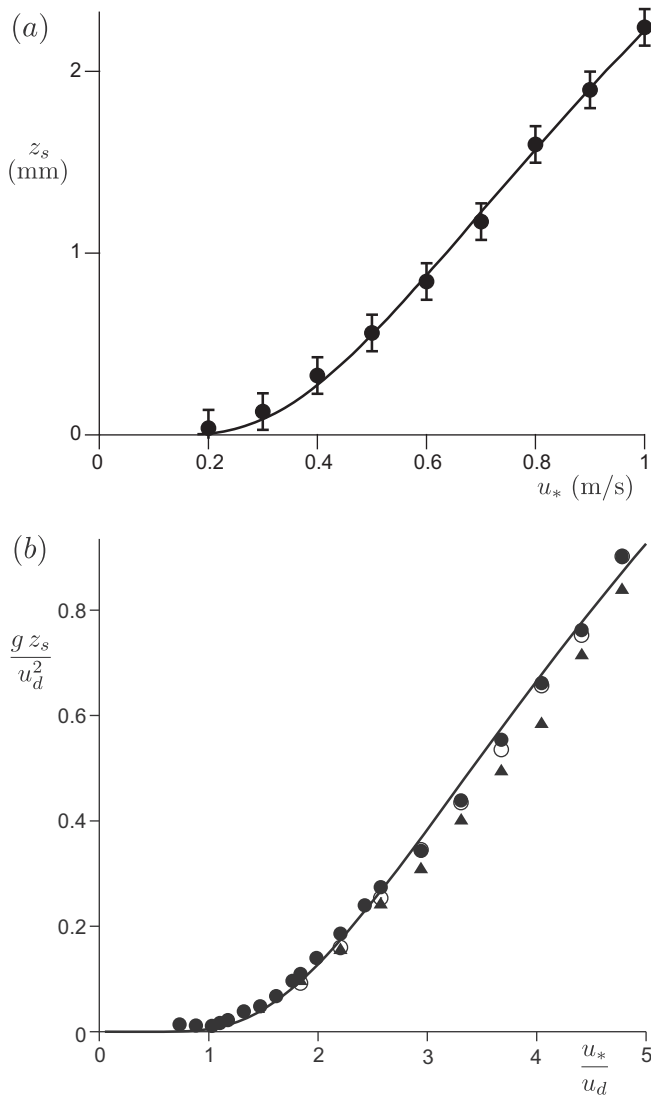
Fig. 19. (a) Measured aerodynamic roughness length z_s above the transport layer (Rasmussen et al., 1996). (b) Normalized aerodynamic roughness gz_s/u_d^2 as function of the relative shear velocity for different density ratios: $\rho_p/\rho_f = 500$ (○), 1000 (●) and 2000 (▲) (data from numerical simulations). In both cases, the line corresponds to the analytical approximation given in the text (Eq. (53)).

6.3. Grain trajectories

From numerical modeling we can compute the grain trajectories in the steady state, and extract several quantities of interest very close to the bed, where direct measurement is extremely difficult. In Figs. 20 and 21, the horizontal and vertical components of the particle velocity u^p and w^p are displayed for different winds. Note that these figures show the distribution of velocities of grains *at* a given height, while most experimentalists measure the distribution of velocities of grains *crossing* a given height. The latter is obtained from the former by multiplying by the particle vertical velocity. These data show that the upward velocity distribution (positive values of w^p), which results from the splash, is independent of the wind shear velocity. Namikas (2003) and Rasmussen and Sorensen (2008) have shown that a constant vertical launch velocity can be reproduced by field and wind tunnel measurements. In contrast, the negative part of the velocity distribution (downward velocities) exhibits tails that do not collapse for different values of u_*. This results from the effect of the vertical drag force, which is larger for stronger winds. The horizontal velocity
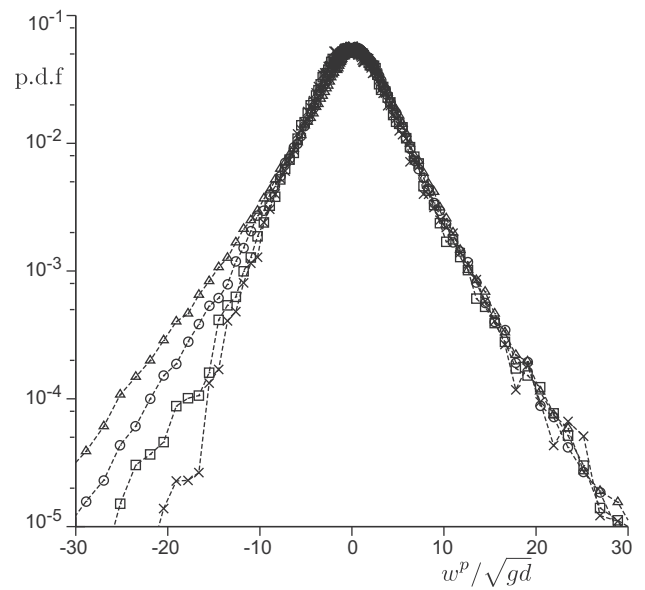

Fig. 20. Distribution of grain vertical velocities at a height $z/d = 5$ (inside the transport layer) for different shear velocities: $u_*/u_d = 2.94$ (×), 4.41 (□), 5.88 (○) and 7.35 (△) (from numerical simulations). Positive values denote upward velocities and negative values downward ones. Upward velocities, resulting from the splash, are independent of the shear velocity. By contrast, downward velocities increase with the wind strength as a direct effect of the vertical wind drag force.

distributions, whether associated to an ascending ($u_\uparrow^p$) or descending ($u_\downarrow^p$) motion, have similar shapes close to the bed, with a data collapse independent of u_* at small velocities, and split tails, which is consistent with grain velocity measurements by Rasmussen and Sorensen (2008).

Wind and particle velocity profiles are displayed in Figs. 22 and 23. They both show a lower zone in which the profiles are independent of the shear velocity, and an upper region where the velocities scale with u_*. This lower zone can be interpreted as the transport layer, as wind reduction resulting from the negative feedback of transport on the flow precisely takes place in this zone. On the contrary, in the upper region, the wind is undisturbed by the presence of moving grains. The transition between these two zones has been named the 'focal' point or region by Bagnold (1941), as it corresponds to the altitude at which all velocity profiles converge. It has been experimentally measured by Zingg (1953), Chepil (1945a,b,c), Horikawa and Shen (1960), Willetts (1983), Rasmussen and Sorensen (2008), and Creyssels et al. (2009) for wind profiles, and Liu and Dong (2004), Rasmussen and Sorensen (2008), and Creyssels et al. (2009) for particle profiles.

6.4. The transport layer and roughness length

We can now characterize in more detail the properties of this transport layer. Its thickness, which is also the vertical location of the focal point H_f, can be estimated as the typical altitude reached by the grains moving within this layer. In the transport layer, the average upward particle velocity $\langle w_\uparrow^p \rangle$ is independent of u_* (Fig. 20) and scales with the threshold u_d. One then obtains the scaling law: $H_f \propto u_d^2/g$. Neglecting the tails of the distributions in Fig. 21, one can similarly express the velocity at the focal point as $U_f \propto u_d$.

Wind tunnel data of Iversen and Rasmussen (1999) can be used to extract measurements at the level of this transport layer (Fig. 24). These experiments have been performed with grain diameters d ranging from 100 to 600 μm. The wind velocity at
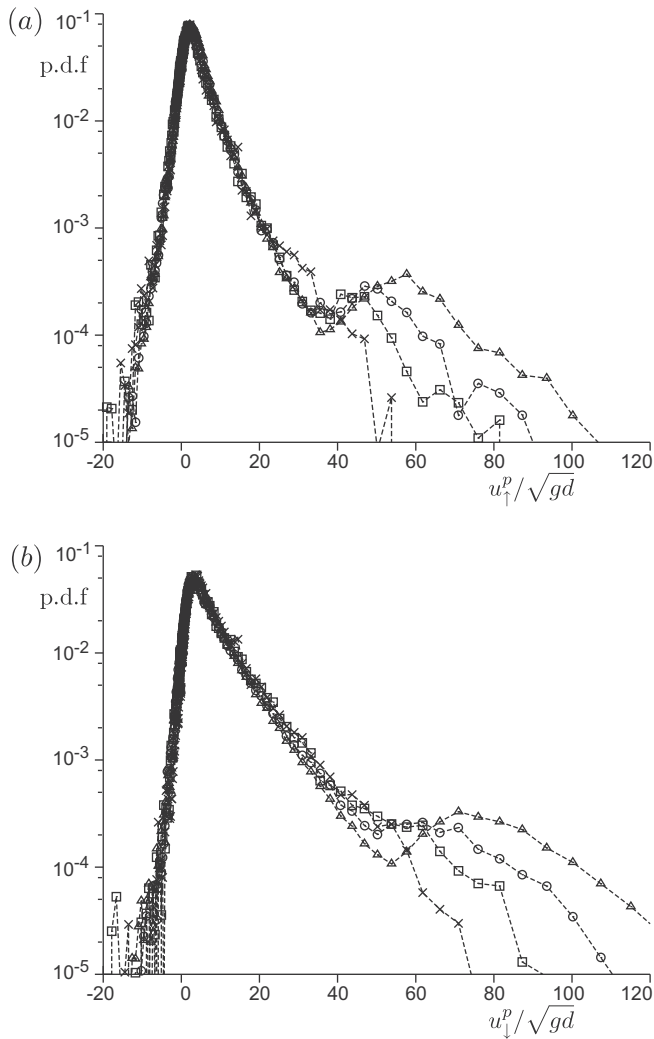
(a)

(b)

Fig. 21. Distribution of grains horizontal velocities at height $z/d = 5$ (inside the transport layer) for different shear velocities: $u_*/u_d = 2.94$ (×), 4.41 (□), 5.88 (○) and 7.35 (△) (from numerical simulations). (a) ejection (or rebound) velocity $u_\uparrow^p$ and (b) impact velocity $u_\downarrow^p$. Impact velocities are typically larger than ejection ones. Note the tail of fast grains whose velocities increase with the wind strength.

the focal point U_f is found to scale with the shear velocity threshold u_d. As shown in Section 5, the scaling with d is more complicated, due to the cross-over between viscous and turbulent regimes. The focal height H_f is found on the order of a centimeter. It varies roughly linearly with the grain diameter d.

Above the transport layer, the undisturbed wind velocity profile should be logarithmic, but with an aerodynamic roughness that depends on the presence of transport: $u(z) = (u_*/\kappa)\ln(z/z_s)$. An expression of this transport roughness length z_s can be obtained by writing the continuity of the velocity profile at the focal point, i.e. $U_f = (u_*/\kappa)\ln(H_f/z_s)$, which can be rearranged to

$$z_s = H_f \exp\left(-\frac{\kappa U_f}{u_*}\right). \tag{53}$$

As shown in Fig. 19, this relationship can reproduce both experimental and numerical results. As expected, z_s is an increasing function of u_*. Other expressions (power laws) have been proposed in the literature, e.g. by Owen (1964) or Raupach et al. (1991) that also fit the experimental data, in particular at large shear velocities (Sherman, 1992; Sherman and Farrell, 2008) (see also Shao (2000, Chapter 6)). However, close to the threshold, the focal point
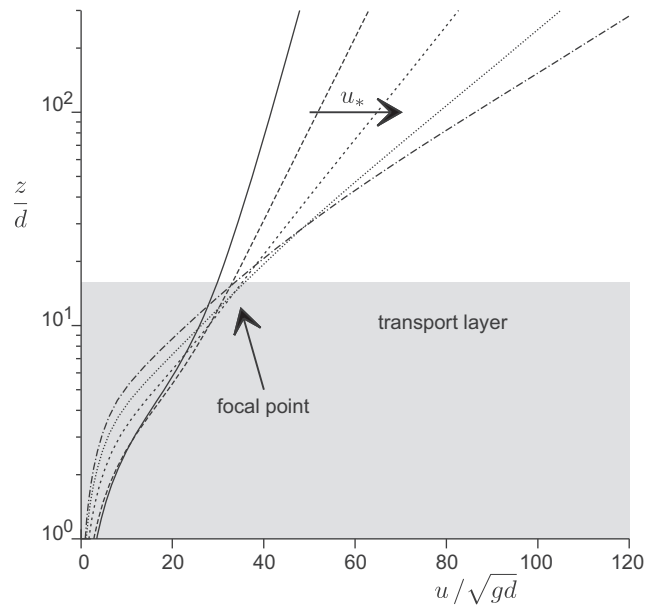

Fig. 22. Vertical profile of the rescaled wind velocity $u/\sqrt{gd}$ for different shear velocities: $u_*/u_d = 1.03$ (full line), 1.84 (long-dashed line), 2.94 (dashed line), 4.42 (dotted line), 5.88 (dot-dashed line) (from numerical simulations). Note the focal point at $z \simeq 15d$.
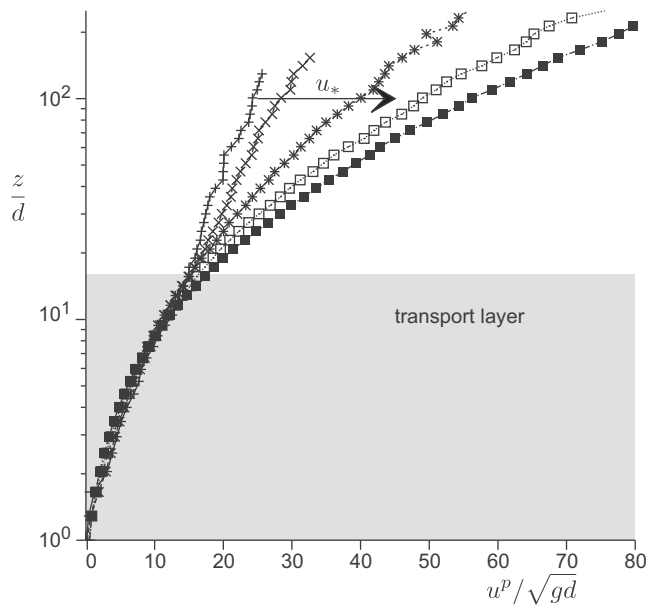
Fig. 23. Vertical profile of the rescaled mean particle velocity $u^p/\sqrt{gd}$ for different shear velocities: $u_*/u_d = 1.17$ (+), 1.47 (×), 2.94 (∗), 4.41 (□) and 5.88 (■) (from numerical simulations). Inside the transport layer $z < H_f \sim 15d$ the average grain velocity is independent of the wind strength. Above it, the grain velocity increases with u_*.

argument gives a much better approximation (Andreotti, 2004; Durán and Herrmann, 2006).

6.5. Flux and volume fraction scaling laws

The fact that, at saturation, the wind is reduced to its threshold in the transport layer independently of the above shear velocity leads to simple scaling laws for the sand fluxes φ_{sat} and q_{sat}, as well as for the particle volume fraction ϕ_{sat}. Assuming that all grain velocities scale with u_d, we can write that $\tau_b = \tau_d = \rho_f u_d^2$ and that $(\langle u_\downarrow^p \rangle - \langle u_\uparrow^p \rangle) \propto u_d$, so that we get from Eq. (51) that
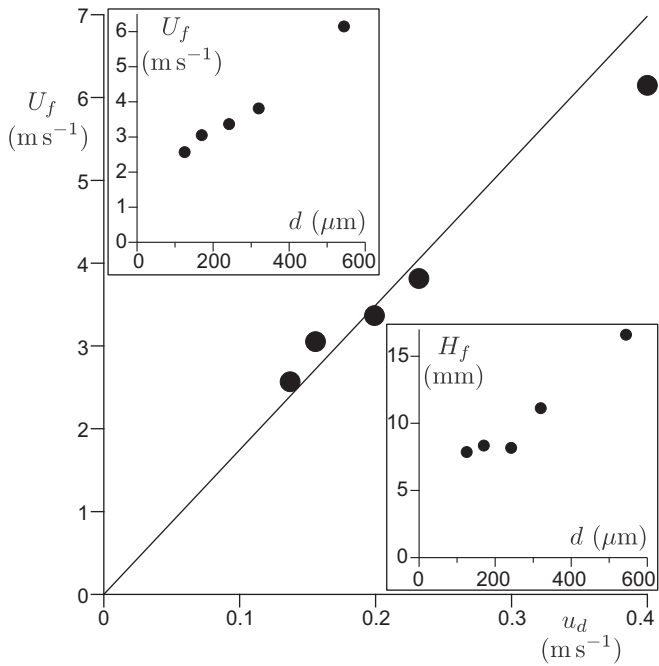
Fig. 24. Experimental data extracted from wind tunnel experiments of Iversen and Rasmussen (1999). Wind velocity at the focal point U_f as a function of the threshold shear velocity u_d. Inlets: scaling of u_d and of the altitude of the focal point H_f with the grain diameter d.

$$\varphi \propto \frac{\rho_f(u_*^2 - u_d^2)}{\rho_p(\langle u_\downarrow^p \rangle - \langle u_\uparrow^p \rangle)} \propto \frac{gd}{u_d}(\Theta - \Theta_d). \tag{54}$$

This expression is reproduced by numerical data, as shown in Fig. 25. Under the same assumption, the average hop length within the transport layer scales as $a \simeq u_d^2/g$, so that the relation $q_{\text{sat}} = a\varphi_{\text{sat}}$ (Section 4) leads to

$$q_{\text{sat}} \propto u_d d(\Theta - \Theta_d). \tag{55}$$

The particle volume fraction close to the bed is related to the vertical flux by $\phi_b = \varphi/\langle w_\uparrow^p \rangle$. Using $\langle w_\uparrow^p \rangle \propto u_d$, the volume fraction vertical profile can be scaled as

$$\phi(z) \propto \frac{gd}{u_d^2}(\Theta - \Theta_d). \tag{56}$$

This linear scaling with the Shields number difference has been reported by Creyssels et al. (2009). In Fig. 26 we show the collapse of the profiles of $\phi(z)$, once rescaled by $(\Theta - \Theta_d)$, obtained from our numerical simulations.

The observed exponential decrease with height suggests a maxwellian distribution of the vertical velocities of the fastest grains. In particular, the characteristic decay length of the exponential profile scales with the width of the distribution of vertical velocities (see Fig. 20): $\langle w_\uparrow^{p2} \rangle - \langle w_\uparrow^p \rangle^2 \sim \langle w_\uparrow^p \rangle^2$ and thus with the mean grain hop height $\langle w_\uparrow^p \rangle^2/g \sim u_d^2/g$, which is by definition the transport layer height.

6.6. Bagnold-like regime

The results presented so far are basically those that can be derived from the Ungar and Haff approach, which is valid under the assumption that all grain velocities scale with the threshold u_d. This assumption is correct if u_* is not too large in comparison to u_d. At large shear velocities, the fast grains above the transport layer, whose velocities scale with u_* (Nalpanis et al., 1993), effectively give a significant contribution to the transport, so that the

Fig. 25. Rescaled vertical flux as function of $\Theta - \Theta_{\text{th}}$ (numerical simulations). Solid-line shows the fit by Eq. (54).
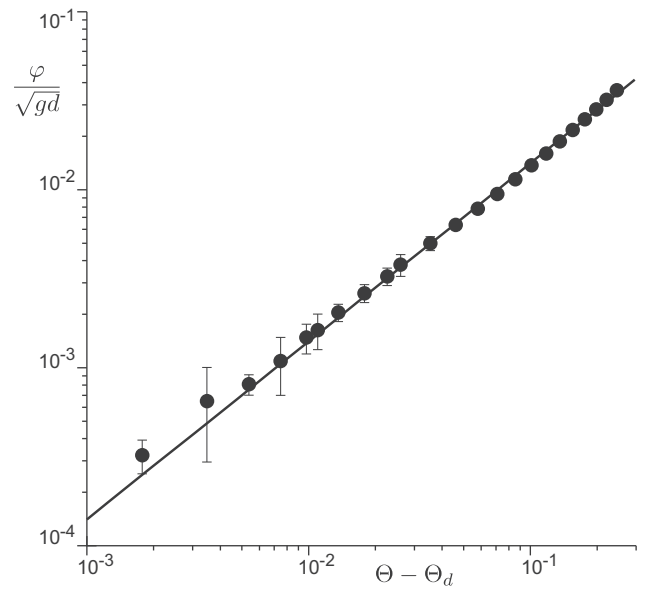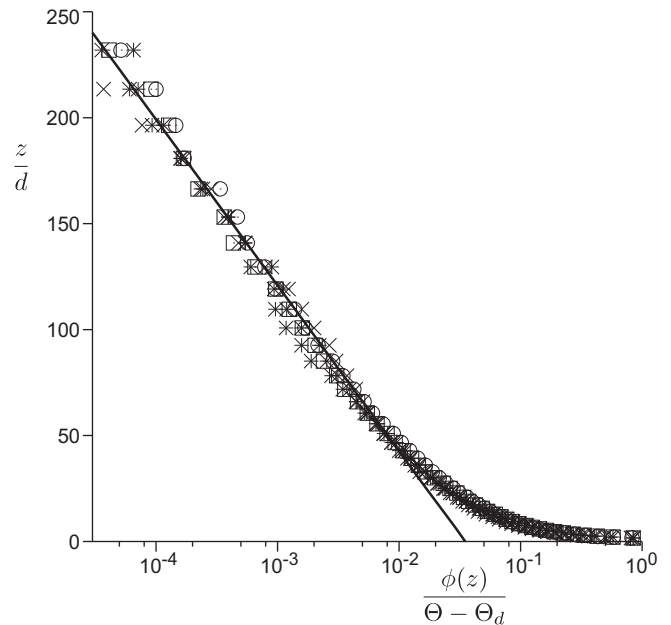

Fig. 26. Vertical profiles of the rescaled volume fraction $\phi/(\Theta - \Theta_{\text{th}})$ for different shear velocities: $u_*/u_d = 2.2$ (+), 2.94 (×), 3.67 (∗), 4.41 (□) and 5.14 (○) (from numerical simulations). Notice the exponential behavior (solid line) at large height with a roughly constant characteristic height.

behavior of the flux with the Shields number is changed to a Bagnold-like scaling:

$$q_{\text{sat}} \propto u_* d(\Theta - \Theta_d) \propto u_d d\sqrt{\Theta/\Theta_d}(\Theta - \Theta_d). \tag{57}$$

Several empirical or semi-empirical expressions for the saturated flux have been proposed in the literature (Bagnold, 1941; Zingg, 1953; Kawamura, 1951; Owen, 1964; Lettau and Lettau, 1978; White, 1979; Sørensen, 1991; Sauermann et al., 2001), which all scale to u_*^3 at large wind shear velocities. In Fig. 27, we display numerical measurements of the saturated flux as a function of the Shields number, up to values where we can see the transition between the two different limits discussed here, i.e. the two different

scalings. Note that, in practice, the transition to the Bagnold-like regime occurs at winds $u_*/u_d \simeq 4$, i.e. larger than ordinary natural field conditions.

In order to provide a more fundamental understanding of this regime, one should go beyond a modeling based on a unique representative type of moving particles, as in the Ungar and Haff picture. Let us then consider two populations of grains in saltation. The first population has trajectories beneath the transport layer, referred to as 'saltons-bottom' (subscript 'bot'). The second population, with trajectories above the transport layer, and thus velocities increasing with u_*, are referred to as 'saltons-top' (subscript 'top'). These two populations are not independent: because at saturation, the average impact velocity, which controls the replacement capacity, must be maintained, one can write the balance

$$\left\langle u_\downarrow^p \right\rangle = n_{\text{bot}} \left\langle u_\downarrow^p \right\rangle_{\text{bot}} + n_{\text{top}} \left\langle u_\downarrow^p \right\rangle_{\text{top}} \propto u_d. \tag{58}$$

In this expression, n_{bot} and $n_{\text{top}} = 1 - n_{\text{bot}}$ are the fractions of 'saltons-bottom' and 'saltons-top' in the total number of grains in saltation, and $\langle u_\downarrow^p \rangle_{\text{bot}}$ and $\langle u_\downarrow^p \rangle_{\text{top}}$, their average impact velocity, respectively. As saltons-bottom move in the transport layer, we have $\langle u_\downarrow^p \rangle_{\text{bot}} \sim u_d$. The estimate of $\langle u_\downarrow^p \rangle_{\text{top}}$ is more subtle. Saltons-top have a velocity u_{top}^p scaling with u_* for most of their trajectory, but once they enter the transport layer, they are slowed down because of a drag force. Their impact velocity can be computed assuming a constant drag coefficient, as

$$u_{\text{top}}^p - \left\langle u_\downarrow^p \right\rangle_{\text{top}} = \frac{(u_{\text{top}}^p - u)^2/u_0}{1 + (u_{\text{top}}^p - u)/u_0}, \tag{59}$$

where $u \simeq u_d$ is the average wind velocity in the transport layer, and u_0 a reference velocity coming from the drag equation ($u_0 \simeq u_d/\Theta_d$). From this expression, one can see that if u_* is close to the threshold u_d, the difference between u_{top}^p and $\langle u_\downarrow^p \rangle_{\text{top}}$ is quadratic in $u_* - u_d$, whereas this difference is linear in u_* for $u_* \gg u_d$.

Recalling that the saturated flux is equal to $a\varphi$, where the scaling of φ with respect to the shear stress and the particle velocities is given in Eq. (54), one must express the hop length a. It is the

product of the hop time by the average velocity. The hop time is related to $\langle w_\uparrow^p \rangle$, and thus independent of u_*, i.e. proportional to u_d/g. Average velocities over the whole grain trajectory can be approximated by those at the top of it, where the grains spends most of the time. Thus, the average velocity is $\langle u^p \rangle \approx n_{\text{bot}} u_{\text{bot}}^p + n_{\text{top}} u_{\text{top}}^p$, where u_{bot}^p and u_{top}^p denote the saltons-bottom and saltons-top velocities are the top of their trajectories, respectively. For the saltons-bottom, the difference between the average and the impact velocity is negligible as both scale with u_d, but for saltons-top it is given by Eq. (59). Therefore, subtracting the average velocity from the average impact velocity (Eq. (58)) and substituting Eq. (59), gives an estimate of the average velocity. We then get,

$$a \simeq u_d/g \left(\left\langle u_\downarrow^p \right\rangle + n_{\text{top}} \left(\frac{(u_{\text{top}}^p - u)^2/u_0}{1 + (u_{\text{top}}^p - u)/u_0} \right) \right). \tag{60}$$

In the limit of large shear velocities ($u_* \gg u_d$) we have $u_{\text{top}}^p \gg u$ and the expression $q_{\text{sat}} \propto a\ (\Theta - \Theta_d)gd/u_d$ gives the scaling law (57). Close to the threshold $u_{\text{top}}^p \sim u$ and Ungar and Haff scaling is recovered as the quadratic correction tends to zero (Fig. 27).

7. Saturation length

Here we discuss in more details the saturation length introduced in Section (4.4). We first report direct as well as indirect measurements of L_{sat}, and then present theoretical arguments to understand the origin and the scaling of this quantity.

7.1. Experimental evidence

Let us consider a sand bed in the half space $x \geqslant 0$, over which wind is blown (sketch in Fig. 28, see also Section 4.4). Upstream of the bed entrance $x = 0$, the bed is non-erodible, but with a similar roughness. In wind tunnel controlled experiments (Andreotti et al., 2010) the longitudinal profiles of the flux $q(x)$ have been obtained with and without an input flux at the upstream bed entrance (Fig. 28). In both cases, the sediment transport increases downstream and further saturates to the same value q_{sat}. The evolution of q can be divided into two phases: a first increase followed by a relaxation phase toward equilibrium. The initial phase is linked to ejection of grains, each saltating grain ejecting a few other grains when it collides with the bed. This results in an exponential increase of the flux (dotted line in Fig. 28). This regime is a
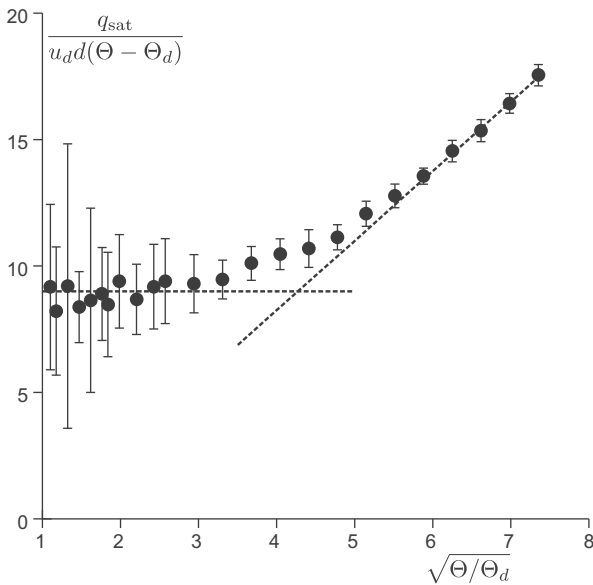

Fig. 27. Rescaled saturated flux obtained from numerical simulations, as a function of $\sqrt{\Theta/\Theta_d} = u_*/u_d$. Close to the dynamic threshold, the mean velocity of the transported particles $u_p \propto q_{\text{sat}}/(\Theta - \Theta_d)$ does not depend on the rescaled shear velocity $\sqrt{\Theta/\Theta_d}$, as predicted in the Ungar and Haff model. Far above the threshold, on the other hand, there is a Bagnold-like regime where the mean velocity increases linearly with the shear velocity.
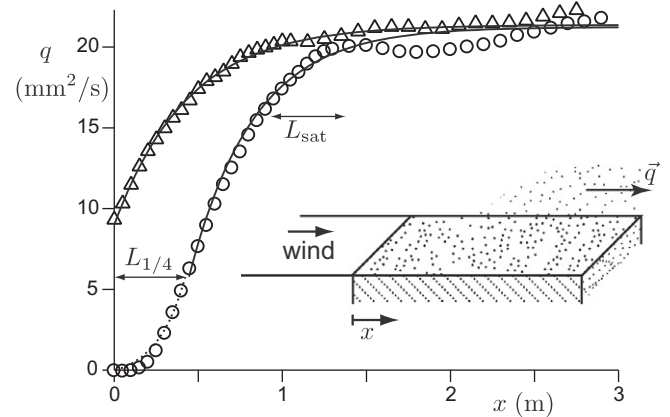
Fig. 28. Spatial variation of the sediment flux over a flat sand bed for $u_* = 0.33$ m/s $\simeq 1.5 u_{\text{th}}$, with ($\triangle$) or without ($\circ$) an input flux. The grain size is $d = 120$ μm. Solid lines: best exponential fit around the saturated state. Dotted lines: initial exponential increase. Inset: sketch of the experiments. The sand bed starts at $x = 0$. $L_{1/4}$ is the length needed before the flux q reaches $q_{\text{sat}}/4$ (from Andreotti et al. (2010)).

priori not taken into account in Eq. (29), which aims to describe the relaxation close to the saturated state. To determine the saturation length, we have thus analyzed the zone where the flux is larger than one fourth of its saturated value q_{sat}. The solid lines in Fig. 28 show the best fit by an exponential law of the form $q_{sat}[1 - e^{-(x-x_0)/L_{sat}}]$, which is the solution of Eq. (29). This forms indicates the magnitude of three parameters: the saturated flux q_{sat}, the saturation length L_{sat} and the position $x = L_{1/4}$ at which the flux reaches the value $q_{sat}/4$.

For different wind strengths, the initial stage, where the flux increases exponentially, is noticeable for weak wind and becomes almost invisible at large wind. This means that the ejection of new sand grains becomes more and more efficient as the flow velocity increases. In contrast, the neighborhood of the saturation is remarkably insensitive to u_*. These qualitative observations are made quantitative by measuring both the length of the initial stage $L_{1/4}$ and the saturation length L_{sat}. One observes in Fig. 29 that $L_{1/4}$ diverges at the threshold and decreases very rapidly with u_*. In contrast, the saturation length L_{sat} is independent of u_*, within error bars. Its average is approximately 55 cm, for sand grains of diameter $d = 120 \pm 40$ μm from the Hostun quarry, with a standard deviation of 10 cm.

It is worth emphasizing the difference between the saturation length L_{sat} and the fetch distance usually defined in the literature (Gilette et al., 1996). Looking at Fig. 28, one could say that, the transport takes between 1 and 2 meters to saturate i.e. to reach a significant fraction of the saturated flux. However, this includes the initial ejection stage, of length $L_{1/4}$ plus a part of the exponential relaxation to equilibrium. L_{sat} characterizes the final stage of the relaxation, which is the only one relevant for dune formation. We have effectively estimated that the sand flux over real dunes is always within 20% of its saturated value. Note finally that L_{sat} is much shorter than the apparent fetch distance (typically 40 cm for Fig. 28).

Another way to measure the saturation length is based on the wavelength at which dunes form by instability. The theoretical prediction of the wavelength at which dunes emerge from a flat sand bed has been progressively refined since the first linear stability analysis of Andreotti et al. (2002b). It is based on two separate stages. First, one needs to perform the hydrodynamical calculation of the turbulent velocity field around obstacles of small amplitude (Jackson and Hunt, 1975; Hunt et al., 1988; Richards, 1980). One
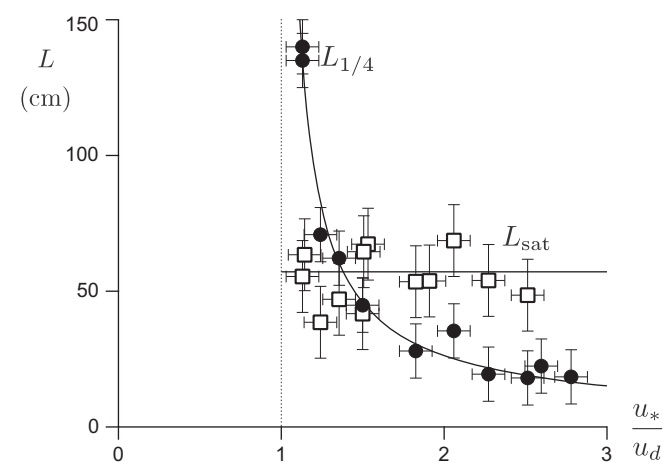
extracts from this heavy calculations the components of the basal shear stress in phase and in quadrature with the elevation profile, as a function of the ratio of the wavelength λ to the aerodynamic roughness z_0. The most recent and detailed calculation has been performed by Fourrière et al. (2010). In particular, the robustness of the results with respect to turbulence modeling has been systematically tested. Second, one needs to describe the sand transport around the saturated state, and this is where the saturation length is important. The outcome of the linear stability analysis of such a model gives the relation between the wavelength of the most unstable mode, the saturation length, and the other parameters. It follows that the prediction of this emerging wavelength is essentially governed by L_{sat} and not sensitive to the formula used for the relationship between the saturated flux and the basal shear velocity.

Barchan flanks provide a good place to see the emergence of the dune instability, as shown in Fig. 30a. The topography as well of the flux is modulated at a wavelength typically around 20 m (Fig. 30b) (Elbelrhiti et al., 2005). Inverting the theoretical relation relating this wavelength to L_{sat}, one can then deduce the saturation length in an indirect way. Other similar data, corresponding to various wind velocities, have been used by Andreotti et al. (2010). Fig. 30 shows that this independent determination of L_{sat} agrees with the direct one, once rescaled: L_{sat} is around $2(\rho_s/\rho_f)d$, within a 50% dispersion.

Fig. 29. Direct measurements of the saturation length L_{sat} and of the ejection length $L_{1/4}$ as a function of the wind shear velocity u_*, rescaled by the threshold u_d. By definition, $L_{1/4}$ is the length needed before the flux q reaches $q_{sat}/4$; L_{sat} is the relaxation length close to the saturated state. The solid lines are, respectively, the best fit by a constant and by a power law diverging at the threshold. Data from Andreotti et al. (2010).

Fig. 30. (a) Waves on the flanks of a barchan dune. The saturation length L_{sat} can be calculated indirectly from the relative amplitude δh of this waves and the perturbation they induce on the flux δq (b). (c) Saturation length L_{sat}, rescaled by the drag length $\rho_s/\rho_f d$, as a function of the wind shear velocity u_*, rescaled by the threshold u_{th}. Direct measurements, performed in a wind tunnel (♦) and in the field (△), are compared to those determined from the initial dune wavelength (storms: (☆) and slipfaceless dunes (○)).

7.2. Modeling the saturation length

To understand the origin of the saturation length for aeolian transport, it can noticed that the flux can be written as the product of a density of transported grains and a speed. Therefore, two mechanisms may limit saturation. First, the grains must be accelerated until they reach the speed of flow. Second, the erosion of the bed must increase the number of transported grains up to its saturated value. To describe the first mechanism, we consider the horizontal movement of a single grain accelerated by the wind turbulent drag force:

$$\frac{du^p}{dt} = \frac{3}{4} \frac{C_d \rho_f}{\rho_p d} (u - u^p)^2. \tag{61}$$

Assuming a constant drag coefficient for simplicity, this equation can be integrated analytically, and this shows that the relaxation of the particle velocity to fluid velocity occurs over a length which varies as

$$L_{sat} \sim \frac{\rho_p}{C_d \rho_f} d, \tag{62}$$

with a proportionality factor of order 2 (Andreotti et al., 2002a; Andreotti, 2004).

Let us study now the second mechanism related to transient saturation of the number of grains, assuming that the grains instantaneously reach the flow speed. Consider for instance the case in Fig. 28 where the sand bed starts at $x = 0$. After the first grain is ejected, it flies, collides with the bed and eject others grains. These are themselves accelerated by the wind, collide with the ground and activate other grains. This amplification can be described by a replacement capacity N_C. It is a function of the average grain impact velocity, which is itself a function, *via* the grain trajectories, of the wind speed in the transport layer. For simplicity, one can write N_C as a function of the basal stress τ_b. Thus at each jump of length a, the number of grains transported is multiplied by $N_C(\tau_b): q(x + a) = q(x)N_C$. In the continuous limit, this relationship becomes

$$a\frac{dq}{dx} = (N_C(\tau_b) - 1)q. \tag{63}$$

The characteristic length of the first regime of exponential growth is then $a/(N_C(\tau_b) - 1)$. In the initial phase of amplification, there are only a few grains in motion so that τ_b is simply equal to the unperturbed wind shear stress τ.

Now consider the final phase of the transient saturation, when the flow has almost reached its saturated value. The basal stress is then close to the threshold stress τ_d. One can expand N_C and the evolution of the flow is then governed by the equation

$$a\frac{dq}{dx} \simeq q_{sat} \frac{dN_C}{d\tau}\bigg|_{\tau_d} (\tau_b - \tau_d). \tag{64}$$

Notice that τ_b and q are related one to each other (Eq. (51)). For the first order of $\tau_b - \tau_d$, this relationship is expressed as

$$\frac{\tau_b - \tau_d}{\tau - \tau_d} = \frac{q_{sat} - q}{q_{sat}}. \tag{65}$$

After substituting in Eq. (64), we can then obtain the relaxation length of the number of grains transported in the vicinity of the saturated state

$$L_{sat} \sim \frac{a}{\frac{dN_C}{d\tau}\big|_{\tau_d} (\tau - \tau_d)}, \tag{66}$$

which diverges at the threshold of transport and tends rapidly to 0 at high wind (Sauermann et al., 2001).

The saturation length is given as a first approximation by the largest of the two lengths of relaxation that we have calculated above. The spatial relaxation of the flux is thus limited by erosion immediately above the threshold, then very quickly by the inertia of the grains. We can then conclude that as soon as one leaves the immediate vicinity of the threshold, the saturation length is proportional to the density ratio between the grains and the surrounding fluid times the diameter of the grains (Fig. 29).

8. Some open issues on aeolian transport

In this article, we have reviewed the dynamical mechanisms controlling aeolian transport at the scale of the grain and at the scale of the transport layer. We have drawn a coherent picture of the saturated transport and the saturation transient. In this last section, we highlight several issues that we consider to be important and are requiring further research.

8.1. Experimental issues

One of specific problems in the research on aeolian transport is the difficulty to transpose controlled wind tunnel experiments to field behavior. In Section 2, we discussed in detail the difference between the aerodynamics in these two situations, which arises from the very different integral turbulent time-scales: in the wind-tunnel, it coincides with the transport time-scale while in the field, it is 10^3 times larger. The complete understanding of aeolian transport remains spoiled by this issue and there is a need for a convergence of these two situations.

In wind tunnels, most measurements are performed after the sand bed has had time to self-organize, i.e. to form ripples, to present size segregation, etc. To confirm the theoretical ideas presented here, there is a need for data even better than those reported in the literature. In particular, to test more finely the scaling laws with respect to the grain diameter and to the wind speed, transport should be characterized under ideal conditions, using a completely flat bed of quasi mono-disperse rounded particles.

The main controversy on aeolian transport in the field is related to time and space fluctuations of sediment flux. If the nature of the turbulent fluctuations play a minor role, as assumed here, then the flux averaged at the scale of seconds (the transport time scale) on a homogeneous sand bed should be directly related to the wind velocity measured just above the transport layer (and averaged over the same time-scale). The major experimental difficulty to perform this test is to measure the flow velocity at a few centimeters above the sand bed and the transport layer.

8.2. Turbulent fluctuations

An alternative approach is to consider that sand transport is strongly influenced by turbulent fluctuations (Baas and Sherman, 2005; Leenders et al., 2005; Baas, 2008). It has been proposed in subaqueous transport studies that erosion is associated with sediment ejection and sweep (Cellino, 1998; LeLouvetel-Poilly et al., 2009). In the case of saltation, the naive image of coherent structures embedded in the turbulent background and which would entrain grain can be tested by means of resolving sediment flux fluctuations Baas (2004) and Van Boxel et al. (2004) as well as turbulence at the scale of the transport layer. It would then be possible to quantify the possible correlations between the sand flux and the turbulent fluctuations.

Another possible role of turbulent fluctuations is to induce randomness in the drag force exerted by the fluid on the particles. When the order of magnitude of this force is larger than gravity, saltation is replaced by turbulent suspension (Cierco et al., 2008).

The nature of this transition – Is it progressive or sudden, when the wind strength is increased? – is still uncertain, along with the influence of fluctuations on the saturated flux (Anderson et al., 1991). One of the expected outcomes of this approach to turbulent suspension is the divergence of the saturation length (Claudin et al., 2011).

Turbulent fluctuations have a significant effect in the presence of gradients along the direction transverse to wind velocity, for instance along the flanks of dunes. When the flow is not homogeneous anymore, a transverse component of the saltation flux will be present. In the turbulent regime, the trajectory of the grains are effectively erratic, due to wind turbulent fluctuations. In between two collisions with the bed, the grains are randomly deflected in the transverse direction with an average angle β around the mean direction of the wind. According to our own field measurements, β is approximately equal to 20°. Along the transverse direction, the grains thus follow a random walk with a mean free path $l \sim \beta a$, where a is the average hop length.

Consider a flow with a speed along the x axis whose magnitude depends on the transverse direction y. Higher wind velocities imply more saltating grains. Thus, the net transverse flux q_y is proportional to $q_x(y - 1/2) - q_x(y + 1/2)$, as more grains will travel from the region of large concentration (larger flux) to the region of low concentration (smaller flux). This analysis leads to a scaling law connecting q_y to q_x and to the average hop length a of the type:

$$q_y = -\beta a \frac{\partial q_x}{\partial y}. \tag{67}$$

The mass conservation Eq. (27) in the case of an almost parallel flow but transversally heterogeneous, thus reads

$$\frac{\partial \zeta}{\partial t} + \frac{\partial q_x}{\partial x} = \beta a \frac{\partial^2 q_x}{\partial y^2}. \tag{68}$$

This expression can be easily adapted to a three dimensional situation. Let us emphasize that the term on the right hand side is purely a turbulent effect and does not result from the surface slope. Its presence has an influence on the shape of dunes as it introduces a coupling transverse to the wind. In particular, such an effect provides a simple, but not unique, explanation of the crescentic shape of barchan dunes (Kroy et al., 2005). Alternative explanations are based on a different phenomenology for the coupling between longitudinal and transversal flows. Instead they consider the transversal deformation of the wind, and thus the flux, due to the three dimensional topography, and/or the effect of gravity on lateral flows due to the inclination of the bed (Hersen et al., 2004; Schwämmle and Herrmann, 2005). The latter still requires further research.

8.3. Influence of bed slope on the saturated flux

In Section 5.4, the effect of a longitudinal bed slope on the transport threshold was discussed: it increases on upward slopes as stronger flows are needed to dislodge a grain, while it decreases on downward slopes due to the opposite effect. Following the same reasoning, as suggested by the relation between the saturated flux and the transport threshold, q_{sat} must increase/decrease on downward/upward slopes. However, empirical evidence from wind tunnel measurements (Iversen and Rasmussen, 1999) show that the full extend of this modification is not captured by the direct substitution of the flat bed transport threshold $\Theta_d(0)$ with the modify one $\Theta_d(\alpha)$. The empirical data is effectively consistent with a further substitution of the gravity acceleration g by $g(\cos\alpha + \sin\alpha/\mu)$ which gives a modified saturated flux of the form:

$$q_{sat}(\alpha)\left(\cos\alpha + \frac{\sin\alpha}{\mu}\right) = u_d(\alpha)d(\Theta - \Theta_d(\alpha))f(\Theta), \tag{69}$$

where f is a function of the Shields number. As shown in Section 6.5, f is constant in the Ungar and Haff regime, while in the Bagnold's regime $f \propto \sqrt{\Theta/\Theta_d(\alpha)}$.

Based on their experimental results, Iversen and Rasmussen (1999) have introduced the above scaling for the flux through a Bagnold-like argument, based on a picture valid for subaqueous bed load transport. However, in the context of aeolian transport, where the most important contribution to the flux comes from grains in saltation, the extra multiplicative term $(\cos\alpha + \sin\alpha/\mu)$ applied to q_{sat} is not well understood. The fact that this extra terms involves the effective friction coefficient μ introduced for the dynamic threshold $\Theta_d(\alpha)$ is puzzling, since the processes are fundamentally different: the modification of the threshold comes from the force balance on a grain resting at the bed, while the modification of the flux is related to the trajectories of flying grains.
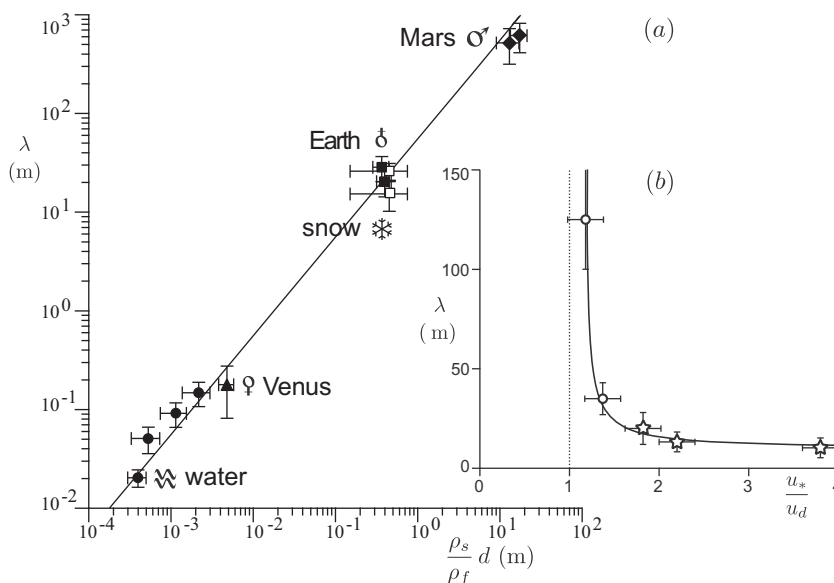

Fig. 31. (a) Measured wavelength λ of elementary dunes, formed by linear instability, as a function of the grain to fluid density ratio multiplied by the grain size. (b) Measured wavelength λ as a function of the rescaled wind velocity, for aeolian dunes composed by 180 μm grains.

A tentative explanation for the origin of this scaling can be found in the different behavior of saltating grains, which follow the wind, and grains in reptation, which are more sensitive to the bed slope (Howard, 1977; Andreotti, 2004; Hersen et al., 2004). Assuming that both fluxes are proportional, the saltation flux would have an equivalent form $q_{sat}(\cos\alpha + \sin\alpha/\mu_R)$ (see Eq. (69)), where μ_R is a dimensionless constant characterizing the effect of gravity on reptons (Hersen et al., 2004). It sounds plausible that μ_R is given by the inverse friction coefficient μ^{-1} as in Eq. (69). Further study is needed to understand in detail the influence of a longitudinal and a transverse slope on transport.

8.4. Aeolian transport on Mars

The martian atmosphere is composed of CO_2 at low density ρ_f between $1.5 10^{-2}$ and $5 10^{-2}$ kg/m³. The photographs taken by the rovers mostly show a bi-disperse material: large spheres of millimetric scale, composed of hematite ($\rho_p = 5270$ kg/m³) and small basalt grains ($\rho_p = 3010$ kg/m³) with iron coating between 60 and 110 μm (Andreotti and Claudin, 2007). The rough estimates of grain size on dunes, based on thermal diffusion, overestimate this observation by a factor of two (Fenton, 2003; Fenton and Mellon, 2006; Fergason et al., 2006; Jerolmack et al., 2006). Assuming that the grains transported have a size comparable to those on Earth or smaller, the main difference between saltation on Mars and on Earth is the density ratio ρ_p/ρ_f.

On Earth, ρ_p/ρ_f is around 2.2×10^3, the static threshold Shields number is around 0.03 and the dynamic threshold Shields number around 0.01. Using Eq. (46), one obtains a value for the coefficient b of approximately 30. On Mars, where the density ratio is around 1.6×10^5, the static threshold Shields number should be similar. However, the collision process is not sensitive to the fluid density. Using again Eq. (46), one obtains a dynamic threshold Shields number around 2×10^{-4}. In other words, the actual threshold velocity on Mars would be only $\simeq 1.4$ times larger than on Earth. Further studies are required to investigate the details of planetary transport.

The main issue is the different scaling laws with the density ratio ρ_p/ρ_f. It has been shown that the wavelength at which dunes form scales on ρ_p/ρ_f (Hersen et al., 2002; Claudin and Andreotti, 2006) (see Fig. 31). They are thus 80 times larger on Mars than on Earth,
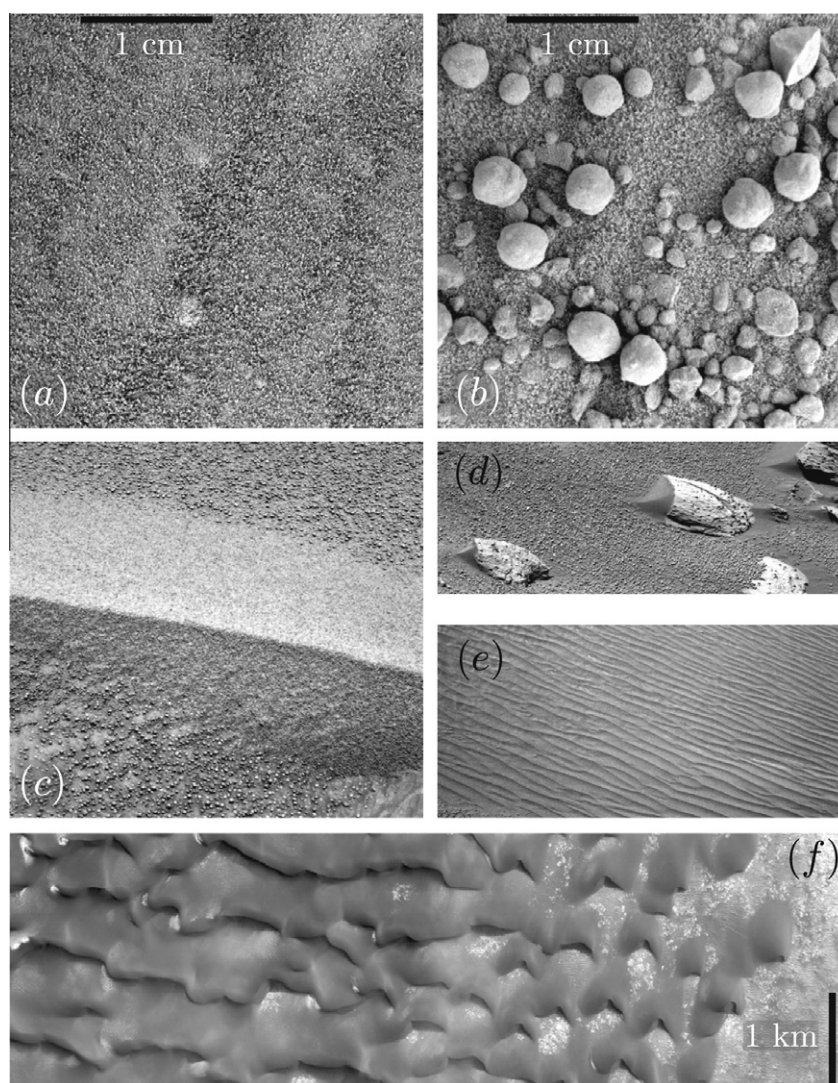

Fig. 32. Grain, ripples and dunes on Mars. (a) Microscope photograph of the sand on a Martian ripple. (b) Microscope photograph showing the mixing of small grains and hematite spherules 'blueberries', characteristic of the soil seen by the two rovers. (c) Aeolian ripple on Mars, characteristic of transport in saltation. A strong difference of composition between the soil covered by blueberries and the ripple can be observed. (d) Aeolian shadow dunes on Mars, characteristic of transport in saltation. These shadow dunes behind stones are clearly evidencing that small grains are transported in saltation, but not the hematite blueberries. (e) Extended zone of Aeolian ripples in a small scale impact crater. Blueberries may be seen at the bottom left of the picture, showing that the ripples are composed of small grains. (f) Aerial view of Kaiser crater elementary dunes.
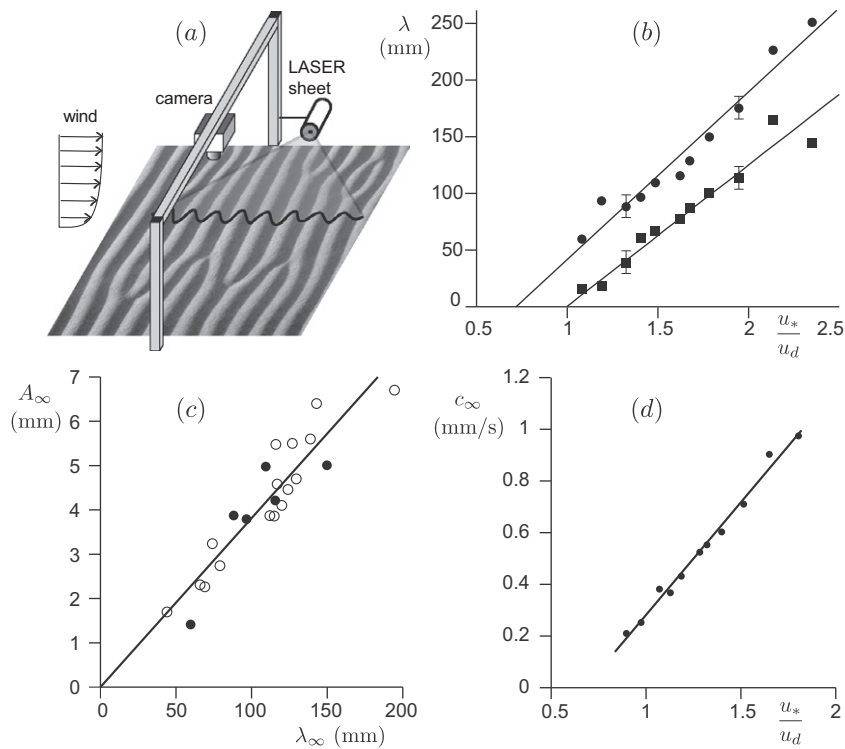
Fig. 33. (a) Experimental set-up used by Andreotti et al. (2006) in the field and in a wind tunnel to study aeolian ripples. The inclined laser sheet allows measurement of the wavelength λ, the amplitude A and the velocity c from a pair of images. (b) Initial ($\square$) and final ($\bullet$) wavelengths as a function of the rescaled wind velocity. (c) Amplitude of mature ripples as a function of the wavelength in the field ($\bullet$) and in a wind tunnel $\circ$. (d) Propagation speed as a function of the rescaled wind velocity.
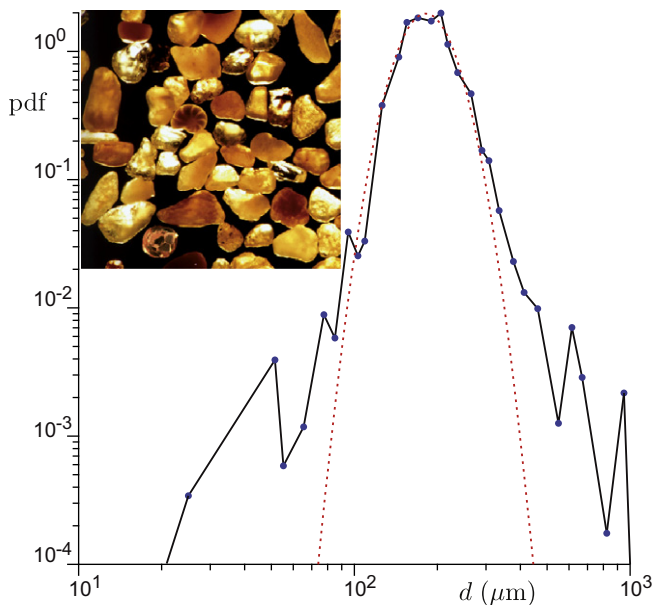

Fig. 34. Typical grain size distribution of an aeolian dune in the Atlantic Sahara. Technically, the graph shows the probability distribution function ($p \cdot d \cdot f$) of $\log(d)$, weighted in mass. The dotted line shows the best fit by a log-normal distribution, which appears as a parabola in this log–log plot.

Fig. 35. Wind tunnel measurement of the spatial growth of the mass flux by a strong wind (22 m/s in the center of the wind tunnel). Data from Dong et al. (2004). The linear regression is shown as a reference.

where kilometer scale giant dunes result from pattern coarsening and not from a linear instability (Andreotti et al., 2009). On the other hand, from previous arguments (see Section 5.3), the threshold velocity u_d is almost independent on ρ_p/ρ_f so that the transport layer is expected to remain at centimeter scale. Recent numerical simulations of Mars transport by Kok (2010) confirm this analysis. Other models based on a maximum principle rather than a balance between erosion and deposition have suggested that, on the contrary, saltation is 'giant' on Mars i.e. with all the lengths multiplied by ρ_p/ρ_f (Almeida et al., 2008). Future work is required to discriminate between these possibilities (see Fig. 32).

8.5. Aeolian ripples

The formation of aeolian ripples is intimately related to sand transport. It is widely accepted that they emerge due to the

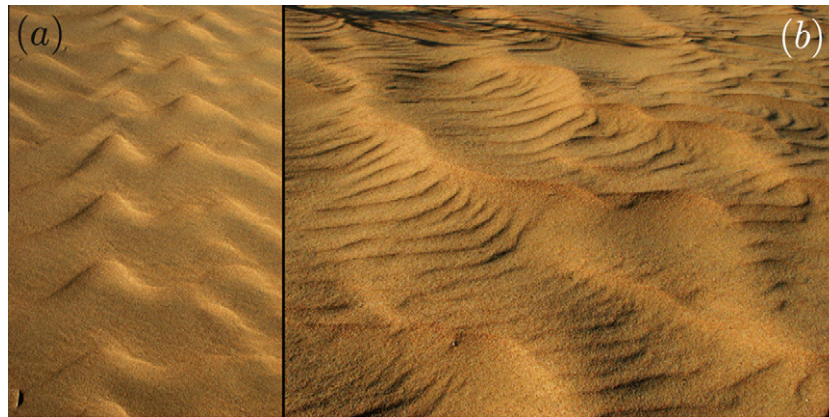**Fig. 36.** Patterns due to segregation between coarse and fine grains. (a) When coarse grains do not cover the sand bed surface, they collect into 'chiflones' which are crescent shape structures aligned along the wind direction. (b) When coarse grains cover the surface, they form mega-ripples, which present simultaneous patterns at different length-scales.

collision of saltons on the bed and the resulting motion of reptons (Anderson, 1987, 1990; Terzidis et al., 1998; Prigozhin, 1999; Csahók et al., 2000; Yizhaq et al., 2004). Therefore, they provide a unique way to test models against observations. As they are much larger than the saltation layer and as they form and move with a much larger time-scale, they are easy to measure. In the Ungar and Haff regime, the characteristics of the grain population that dominate transport (trajectories and velocities) is independent of u_*. This suggests that the growth rate of aeolian ripples must increase with u_* as the impacting flux increases. However, one expects the length at which aeolian ripples form to be independent of u_*. This is not what controlled field and wind tunnel experiments performed by Andreotti et al. (2006) show: the wavelength at which ripples form actually increases linearly with u_* (see Fig. 33 for a summary of ripple scalings). This strongly suggests that a fundamental ingredient is missing in the existing models of ripples instability. Further studies will have to revisit aeolian transport and instability mechanisms to explain this discrepancy.

8.6. Polydisperse sand beds, aeolian sieving and mega-ripples

In contrast to subaqueous bedforms, aeolian dunes are usually composed of quasi-monodisperse sand (Fig. 34). The processes by which this so-called aeolian sieving takes place are currently not understood nor modeled. They may still be important in some situations, and in particular by strong wind. Fig. 35 shows a wind tunnel measurement of the saturation transient performed at a shear velocity u_* more than three times larger than the threshold u_d. Even with a 16 m long wind tunnel, the flux does not saturate (Shao and Raupach, 1992; Gilette et al., 1996), while 2 m are sufficient at lower wind velocities. We have ourselves observed such unusual fetch distances, in similar conditions, associated with a change of sand bed composition: a larger and larger fraction of large grains was observed as a function of the distance to the wind tunnel entrance. Another possible origin of this apparent increase of the saturation length L_{sat} would be the transition from saltation to suspension (Claudin et al., 2011). Many dunes are covered in surface by coarse grains which form either chiflones or mega-ripples, depending on the fraction of the surface covered (Fig. 36). As there is no real understanding of the segregation processes, these structures have not received any correct explanation so far.

Acknowledgments

Appendix A. Aerodynamical forces in unsteady heterogeneous flows

In this appendix, we discuss in more detail some of the aerodynamical forces that act on grains in unsteady heterogeneous flows. These forces are in addition to the drag force, which is usually the only one considered for simplicity.

A.1. Archimedes force

The Archimedes force results from the stress which would have been exerted on the particle, if the particle had been a fluid. To compute it, one does not take into account the disturbances of the flow induced by the particle. The force is thus the integral over the surface of the fluid stress $\vec{F}_{\text{Archimedes}} = \oint \sigma \vec{dS}$, where σ_{ij} is the undistorted fluid stress tensor. This expression can be rewritten as an integral over the volume of the particle $\int \text{div}\sigma dV$, which can be estimated using the equations of motion of the fluid.

$$\rho_f \frac{d\vec{u}}{dt} = \rho_f \vec{g} + \text{div}\sigma. \tag{A.1}$$

The Archimedes force $\vec{F}_{\text{Archimedes}}$ is thus equal to

$$\vec{F}_{\text{Archimedes}} \simeq \frac{\pi}{6} \rho_f d^3 \left(\frac{d\vec{u}}{dt} - \vec{g} \right), \tag{A.2}$$

where, in first approximation, the quantities are evaluated for the undisturbed flow, at the center of the grain. In the case of the grain falling in a fluid at rest, the effect of the undisturbed flow reduces to the buoyancy force. When particles and fluid do not have the same density, the acceleration term makes the grain not to follow the main flow direction. Consider the important example of a vortex inside a turbulent flow. The rotating fluid is locally at equilibrium between the centrifugal force and the pressure gradient. A grain denser than the fluid, passing through the vortex core, is submitted to a centrifugal force larger than the displaced fluid but at the same pressure gradient. It is thus ejected from the vortex zone. This effect explains the dust devil phenomenon: mini-tornadoes of convective origin are surrounded by a tube of dust. Another consequence is that a turbulent flow cannot mix dense particles effectively (Bec et al., 2007, 2010). Rotation-free regions therefore have a higher concentration of particles than the average value.

A.2. Added-mass force

A second contribution to the hydrodynamical force is applied due to the relative acceleration between the fluid and the particle. For example, when a particle accelerates in an immobile fluid, the instantaneous force at time t is not the force previously computed for the steady motion of velocity $\vec{u}^p(t)$. A further force is required to accelerate the fluid around the particle. This additional mass force reads (Brennen, 1982).

$$\vec{F}_{\text{addedmass}} \simeq \frac{\pi}{12} \rho_f d^3 \left(\frac{d\vec{u}^p}{dt} - \frac{d\vec{u}}{dt} \right). \quad (A.3)$$

The particle had an effective mass

$$m_{\text{effective}} \simeq \frac{\pi}{6} \left(\rho_p + \frac{1}{2} \rho_f \right) d^3 \quad (A.4)$$

and the displaced fluid an effective mass $\frac{\pi}{4} \rho_f d^3$. Hence the name 'added mass' for this inertial effect.

A.3. Basset force

The third effect (Basset force) results from the delay between the time at which a particle changes its relative velocity with respect to the fluid, and the time at which the force changes. At the linear order, one can describe it by a time transfer function

$$\vec{F}_{\text{Basset}} = \int \mathcal{K}(\tau) \frac{d\vec{F}_d}{dt} (t - \tau) d\tau. \quad (A.5)$$

The convolution kernel $\mathcal{K}(\tau)$ is a dimensionless function. At low Reynolds number, the boundary layer is viscous so that the delay results from the diffusion of momentum between the surface of the grain and the flow. Dimensionally, the kernel is thus a function of $d/(\sqrt{\nu\tau})$. The rigorous calculation at low Reynolds number gives a kernel reflecting long time correlations:

$$\mathcal{K}(\tau) = \frac{1}{2\sqrt{\pi}} \frac{d}{\sqrt{\nu\tau}}. \quad (A.6)$$

At high Reynolds number, the boundary layer is turbulent so that the delay results from the momentum convection time. The kernel is then a function of $d/(|\vec{u}^p - \vec{u}|\tau)$. In the cross-over between these asymptotic regimes, the grain emits an unsteady wake composed of vortices, so that, the Basset correction cannot be written as a time independent transfer function.

A.4. Magnus force

For a homogeneous flow, when a grain is nonetheless moving at the velocity $\vec{u}^p$ but rotates at the angular velocity $\vec{\Omega}$, a force perpendicular to $\vec{u}^p$ and to $\vec{\Omega}$ appears, which reads

$$\vec{F}_m = \frac{\pi}{8} C_m \rho_f d^3 \vec{\Omega} \wedge (\vec{u}^p - \vec{u}), \quad (A.7)$$

where C_m is a constant. This so-called Magnus force can simply be interpreted as a pressure balance around the grain. Let us consider the frame of reference which moves with the grain at the velocity $\vec{u}^p$ (Fig. A.37). When the grain rotates at the velocity $\vec{\Omega}$, the fluid velocity is increased on one side and decreased on the other. The Bernoulli relation shows that a higher (resp. lower) velocity leads to a lower (resp. higher) pressure. The Magnus force results from this asymmetry of the pressure field. At low Reynolds number, C_m can be approximated using asymptotic matching techniques, which give $C_m \simeq 1$ (Rubinows and Keller, 1961). Note that the lift force is to a large degree determined by asymmetries in the position of or in the fluctuations of the separation line, and this depends considerably on the irregular shape of sand grains. Therefore, formulae for
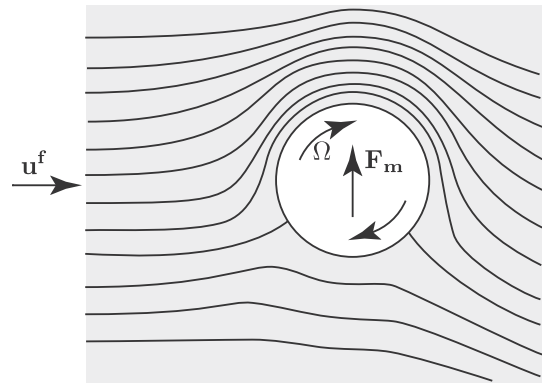

Fig. A.37. Streamlines around a sphere rotating at the angular velocity Ω, in the frame of reference of the particle. $\vec{F}_m$ is the Magnus lift force.

spheres must be applied to natural sand grains with some care. White and Schulz (1977) have investigated the magnitude of the Magnus force on aeolian saltons.

A.5. Equation of motion

In summary, the equation of motion for a sphere at low particle Reynolds number, in a flow which does not vary at scale d reads (Mordant and Pinton, 2000)

$$\left(\rho_p + \frac{1}{2} \rho_f \right) \frac{d\vec{u}^p}{dt} = (\rho_p - \rho_f)\vec{g} + \frac{3}{2} \rho_f \frac{d\vec{u}}{dt} + \frac{3}{4} C_d(\mathcal{R}) \rho_f$$
$$\times \frac{|\vec{u} - \vec{u}^p|(\vec{u} - \vec{u}^p)}{d} + \frac{6\vec{F}_{\text{Basset}}}{\pi d^3} + \frac{3}{4} C_m \rho_f \vec{\Omega}$$
$$\wedge (\vec{u}^p - \vec{u}), \quad (A.8)$$

where the left side and the first two terms on the right side result from the grain acceleration, from Archimedes force and from the added mass force. The other terms are the drag force, the Basset force and the Magnus force. Note that for the sake of simplicity, most aeolian models only consider the hydrodynamic drag force.

A.6. Force in a shear flow

Let us finally consider the case of a flow inside which the velocity field varies at the scale of the diameter d (Matas et al., 2004). In the first order, the force is modified by the velocity gradient. In the case of a shear flow of shear rate ω, a lift force has been calculated by Saffman at low Reynolds number

$$\vec{F}_s = \alpha_s \rho_f d^2 \sqrt{\nu\omega} \vec{u}^p, \quad (A.9)$$

with $\alpha_s \simeq 1.61$ for a sphere. This force results, like the Magnus force, from the asymmetry of the pressure field induced by the grain rotation. It is an inertial effect which vanishes at zero Reynolds number.

At high Reynolds number, the lift force does not depend on viscosity anymore. Dimensionally, one can write an expression very similar to Magnus force,

$$\vec{F}_s = \frac{\pi}{6} C_m \rho_f d^3 \vec{\omega} \wedge (\vec{u}^p - \vec{u}), \quad (A.10)$$

where $\vec{\omega} = \vec{\nabla} \wedge \vec{u}$ is the fluid vorticity and C_L the lift coefficient. Bagnold (1974) and Willetts and Murray (1981) investigated the magnitude of this force experimentally and Owen (1964) theoretically. According to Moraga et al. (1999), the lift coefficient is a function of the Reynolds number $\mathcal{R}_s = \sqrt{\omega d |\vec{u}^p - \vec{u}| d / \nu}$. Below $\mathcal{R}_s \sim 10^2$, the lift coefficient is controlled by the pressure asymmetry and is positive. The best fit to experimental data gives a lift coefficient equal to $C_L \simeq 0.12$. Measurements performed by analyzing the

motion of bubbles in turbulent pipe flow give $C_L \simeq 0.25$ (T, 2010). These values are smaller than expected from inviscid calculations ($C_L = 0.5$), which ignore wake effects. Above $\mathcal{R}_s \sim 10^2$, the lift coefficient is controlled by vortex shedding and is negative. Around $\mathcal{R}_s \sim 10^3$, the experimental data of Moraga et al. (1999) give a lift force coefficient around $C_L \simeq -0.17$. Using these values, one finds that the lift force exerted on grains close to the sand bed is at least 10 times smaller than the drag force. This does not preclude larger values of C_L for the grains at rest at the surface of this bed.

The higher order term comes from the velocity field curvature. Expanding the velocity field with respect to the velocity at the center of the sphere, a correction to the Stokes flow, called the Faxén force, can be applied, which depends on the velocity Laplacian:

$$\vec{F}_f = \frac{1}{8}\pi\rho_f \nu d^3 \Delta\vec{u}. \tag{A.11}$$

References

Almeida, M.P., Parteli, E.J.R., Andrade, J.S., Herrmann, H.S., 2008. Giant saltation on Mars. Proc. Natl. Acad. Sci. USA 16, 479–495.

Ammi, M., Oger, L., Beladjine, D., Valance, A., 2009. Three-dimensional analysis of the collision process of a bead on a granular packing. Phys. Rev. E 79, 021305.

Amontons, G., 1699. Moyen de substituer commodément l'action du Feu à la force des Hommes et des Cheveaux pour mouvoir des Machines. In: Histoire de l'Académie Royale des Sciences, 20 juin 1699.

Anderson, R.S., Hallet, B., 1986. Sediment transport by wind: toward a general model. GSA Bull. 97, 523–535.

Anderson, R.S., 1987. A theoretical model for aeolian impact ripples. Sedimentology 34, 943–956.

Anderson, R.S., Haff, P.K., 1988. Simulation of aeolian saltation. Science 241, 820–823.

Anderson, R.S., 1990. Aeolian ripples as examples of self-organization in geomorphological systems. Earth Sci. Rev. 29, 77.

Anderson, R.S., Haff, P.K., 1991. Wind modification and bed response during saltation of sand in air. Acta Mech. 1 (Suppl.), 21–51.

Anderson, R.S., Sørensen, M., Willetts, B.B., 1991. A review of recent progress in our understanding of aeolian sediment transport. Acta Mech. 1 (Suppl.), 1–19.

Andreotti, B., 2004. A two species model of aeolian sand transport. J. Fluid Mech. 510, 47–70.

Andreotti, B., Claudin, P., 2007. Comment on 'Minimal size of a barchan dune'. Phys. Rev. E 76, 063301.

Andreotti, B., Claudin, P., Douady, S., 2002a. Selection of barchan shapes and velocities. Part 1: dynamics of sand, wind and dunes. Eur. Phys. J. B 28, 321–339.

Andreotti, B., Claudin, P., Douady, S., 2002b. Selection of barchan shapes and velocities. Part 2: a two-dimensional modelling. Eur. Phys. J. B 28, 341–352.

Andreotti, B., Claudin, P., Pouliquen, O., 2006. Aeolian sand ripples: experimental evidence of coarsening and saturation. Phys. Rev. Lett. 96, 028001.

Andreotti, B., Fourrière, A., Ould-Kaddour, F., Murray, A.B., Claudin, P., 2009. Giant aeolian dune size determined by the averaged depth of the atmospheric boundary layer. Nature 457, 1120–1123.

Andreotti, B., Claudin, P., Pouliquen, O., 2010. Measurements of the aeolian sand transport saturation length. Geomorphology 123, 343–348.

Baas, A.C.W., 2004. Evaluation of Saltation Flux Impact Responders (Safires) for measuring instantaneous aeolian sand transport rates. Geomorphology 59, 99–118.

Baas, A.C.W., Sherman, D.J., 2005. The formation and behavior of aeolian streamers. J. Geophys. Res. 110, F03011.

Baas, A.C.W., 2008. Challenges in aeolian geomorphology: investigating aeolian streamers. Geomorphology 93, 3–16.

Bagnold, R.A., 1941. The Physics of Blown Sand and Desert Dunes. Chapman & Hall, London.

Bagnold, R.A., 1974. Fluid forces on a body in shear-flow; experimental use of 'stationary flow'. Proc. R. Soc. Lond. Ser. A 340, 147–171.

Bec, J., Biferale, L., Cencini, M., Lanotte, A., Musacchio, S., Toschi, F., 2007. Heavy particle concentration in turbulence at dissipative and inertial scales. Phys. Rev. Lett. 98, 084502.

Bec, J., Biferale, L., Lanotte, A., Scagliarini, A., Toschi, F., 2010. Turbulent pair dispersion of inertial particles. J. Fluid Mech. 645, 497–528.

Bowden, F.P., Tabor, D., 1950. The Friction and Lubrication of Solids I. Clarendon Press, Oxford.

Brennen, C.E., 1982. A Review of Added Mass and Fluid Inertial Forces, Technical Report, CR 82.010, Naval Civil Engineering Laboratory.

Cellino, M., 1998. Experimental Study of Suspension Flow in Open Channel. Doctoral Dissertation No. 1824, Ecole Polytechnique Fdrale, Lausanne, Suisse.

Charru, F., 2006. Selection of the ripple length on a granular bed. Phys. Fluids 18, 121508.

Chepil, W.S., Milne, R.A., 1939. Comparative study of soil drifting in the field and in a wind tunnel. Sci. Agric. 19, 149–257.

Chepil, W.S., 1945a. Dynamics of wind erosion: I. Nature of movement of soil by wind. Soil Sci. 60, 305–320.

Chepil, W.S., 1945b. Dynamics of wind erosion: II. Initiation of soil movement.. Soil Sci. 60, 397–411.

Chepil, W.S., 1945c. Dynamics of wind erosion: III. The transport capacity of the wind. Soil Sci. 60, 475–480.

Cierco, F.-X., Naaim, M., Naaim-Bouvet, F., 2008. Experimental study of particle concentration fluctuations in a turbulent steady flow. Ann. Glaciol. 49, 121–126.

Claudin, P., Andreotti, B., 2006. A scaling law for aeolian dunes on Mars, Venus, Earth, and for subaqueous ripples. Earth Planet. Sci. Lett. 252, 30–44.

Claudin, P., Charru, F., Andreotti, B., 2011. Transport relaxation time and length scales in turbulent suspensions. J. Fluid Mech. 671, 491–506.

Cooke, R., Warren, A., Goudie, A., 1993. Desert Geomorphology. UCL Press, London.

Coulomb, C., 1773. Mémoires de Mathématiques et de Physique Présentés l'Académie Royale des Sciences par Divers Savants et Lus dans les Assemblées, 343, Imprimerie Royale, Paris.

Creyssels, M., Dupont, P., Ould el Moctar, A., Valance, A., Cantat, I., Jenkins, J.T., Pasini, J.M., Rasmussen, K.R., 2009. Saltating particles in a turbulent boundary layer: experiment and theory. J. Fluid Mech. 625, 47–74.

Csahók, Z., Misbah, C., Valance, A., 2000. Dynamics of aeolian sand ripples. Eur. Phys. J. E 3, 71.

Dey, S., 2003. Threshold of sediment motion on combined transverse and longitudinal sloping beds. J. Hydraul. Res. 41, 405–415.

Dong, Z., Liu, X., Wang, H., Wang, X., 2003. Aeolian sand transport: a wind tunnel model. Sediment. Geol. 161, 71–83.

Dong, Z., Wang, H., Liu, X., Wang, X., 2004. The blown sand flux over a sandy surface: a wind tunnel investigation of the fetch effect. Geomorphology 57, 117–127.

Douady, S., Andreotti, B., Daerr, A., 1999. On granular surface flow equations. Eur. Phys. J. B 11, 131–142.

Durán, O., Herrmann, H.J., 2006. Modeling of saturated sand flux. J. Stat. Mech., P07011.

Elbelrhiti, H., Andreotti, B., Claudin, P., 2008. Barchan dune corridors: field characterization and investigation of control parameters. J. Geophys. Res. 113, F02S15.

Elbelrhiti, H., Claudin, P., Andreotti, B., 2005. Field evidence for surface-wave-induced instability of sand dunes. Nature 437, 720–723.

Fenton, L.K., 2003. Aeolian Processes on Mars: Atmospheric Modeling and GIS Analysis. Ph.D. Thesis, Calif. Inst. Technol., Pasadena.

Fenton, L.K., Mellon, M.T., 2006. Thermal properties of sand from Thermal Emission Spectrometer (TES) and Thermal Emission Imaging System (THEMIS): spatial variations within the proctor crater dune field on Mars. J. Geophys. Res. 111, E06014.

Fergason, R.L., Christensen, P.R., Bell III, J.F., Golombek, M.P., Herkenhoff, K.E., Kieffer, H.H., 2006. Physical properties of the Mars Exploration Rover landing sites as inferred from Mini-TES derived thermal inertia. J. Geophys. Res. 111, E02S21.

Ferguson, R.I., Church, M., 2004. A simple universal equation for grain settling velocity. J. Sediment. Res. 74, 933–937.

Finkel, H.J., 1959. The barchans of southern Peru. J. Geol. 67, 614–647.

Fourrière, A., Claudin, P., Andreotti, B., 2010. Bedforms in a turbulent stream: formation of ripples by primary linear instability and of dunes by non-linear pattern coarsening. J. Fluid Mech. 649, 287–328.

Frisch, U., 1996. Turbulence: The Legacy of A.N. Kolmogorov. Cambridge University Press, Cambridge.

Fryberger, S.G., Dean, G., 1979. Dune forms and wind regimes. In: McKee (Ed.), A Study of Global Sand Seas. Geol. Surv. Prof. Pap. 1052, Washington, p. 137.

Garrat, J.R., 1994. The Atmospheric Boundary Layer. Cambridge University Press.

Gilette, D.A., Herbert, G., Stokton, P.H., Owen, P.R., 1996. Causes of the fetch effect in wind erosion. Earth Surf. Processes Landforms 21, 641–659.

Gondret, P., Hallouin, E., Lance, M., Petit, L., 1999. Experiments on the motion of a solid sphere toward a wall: from viscous dissipation to elastohydrodynamic bouncing. Phys. Fluids 11, 643–652.

Gondret, P., Lance, M., Petit, L., 2002. Bouncing motion of spherical particles in fluids. Phys. Fluids 14, 2803–2805.

Goosens, D., Offer, Z., London, G., 2000. Wind tunnel and field calibration of five aeolian sand traps. Geomorphology 35, 233–252.

Greeley, R., Blumberg, D.G., Williams, S.H., 1996. Field measurement of the flux and speed of wind blown sand. Sedimentology 43, 41–52.

Hardisty, J., Whitehouse, J.R.S., 1988. Evidence for a new sand transport process from experiments on Saharan dunes. Nature 332, 532–534.

Harris, R.I., 2008. The macrometeorological spectrum – a preliminary study. J. Wind Eng. Ind. Aerodyn. 96, 2294D2307.

Hastenrath, S.L., 1967. The barchans of the Arequipa Region, Southern Peru. Z. Geomorphol. 11, 300–331.

Hastenrath, S.L., 1987. The barchans of Southern Peru revisited. Z. Geomorphol. 31–32, 167–178.

Hersen, P., Douady, S., Andreotti, B., 2002. Relevant lengthscale of barchan dunes. Phys. Rev. Lett. 89, 264301.

Hersen, P., Elbelrhiti, H., Andersen, K.H., Andreotti, B., Claudin, P., Douady, S., 2004. Corridors of barchan dunes: stability and size selection. Phys. Rev. E 69, 011304.

Ho, T.D., Valance, A., Dupont, P., Ould El Moctar, A., 2011. Scaling laws in aeolian sand transport. Phys. Rev. Lett. 106, 094501.

Horikawa, K., Shen, H.W., 1960. Sand movement by wind action: on the characteristics of sand traps. Technical Memorandum, vol. 119. USACE, Beach Erosion Board.

Howard, A.D., 1977. Effect of slope on the threshold of motion and its application to orientation of wind ripples. Bull. Geol. Soc. Am. 88, 853–856.

Hsu, S.A., 1971. Measurement of shear stress and roughness length on a beach. J. Geophys. Res. 76, 2880–2885.

Hunt, J.C.R., Leibovich, S., Richards, K.J., 1988. Turbulent shear flows over low hills. Q. J. R. Meteorol. Soc. 114, 1435–1470.

Iversen, J.D., Rasmussen, K.R., 1994. The effect of surface slope on saltation threshold. Sedimentology 41, 721–728.

Iversen, J.D., Rasmussen, K.R., 1999. The effect of wind speed and bed slope on sand transport. Sedimentology 46, 723–731.

Jackson, P.S., Hunt, J.C.R., 1975. Turbulent wind flow over a low hill. Q. J. R. Meteorol. Soc. 101, 929–955.

Jensen, J.L., Sørensen, M., 1982. On the mathematical modelling of aeolian saltation. In: Sumer, Müller (Eds.), Mechanics of Sediment Transport. Balkema, Rotterdam, pp. 65–72.

Jensen, J.L., Sørensen, M., 1986. Estimation of some aeolian saltation transport parameters: a re-analysis of Williams data. Sedimentology 33, 547–558.

Jerolmack, D.J., Mohrig, D., Grotzinger, J.P., Fike, D.A., Watters, W.A., 2006. Spatial grain size sorting in eolian ripples and estimation of wind conditions on planetary surfaces: application to Meridiani Planum, Mars. J. Geophys. Res. 111, E12S02.

Jones, J.R., Willetts, B.B., 1979. Errors in measuring aeolian flow by means of an adjustable trap. Sedimentology 26, 463–468.

Johnson, K.L., 1985. Contact Mechanics. Cambridge University Press, Cambridge.

Kamphuis, J.W., 1974. Determination of sand roughness for fixed beds. J. Hydraul. Res. 12, 193–207.

Kawamura, R., 1951. Study on sand movement by wind. Rep. Phys. Sci. Res. Inst. Tokyo Univ. 5, 95–112.

Kind, R.J., 1976. A critical examination of the requirements of model simulation of wind induced erosion/deposition phenomena such as snow drifting. Atmos. Environ. 10, 219–227.

Kolmogorov, A.N., 1941. Dokl. Acad. Nauk USSR 30, 9.

Kok, J.F., Renno, N.O., 2009. A comprehensive numerical model of steady state saltation (COMSALT). J. Geophys. Res. 114, D17204.

Kok, J.F., 2010. Difference in the wind speeds required for initiation versus continuation of sand transport on Mars: implications for dunes and dust storms. Phys. Rev. Lett. 104, 074502.

Kroy, K., Sauermann, G., Herrmann, H.J., 2002a. Minimal model for sand dunes. Phys. Rev. Lett. 88, 054301.

Kroy, K., Sauermann, G., Herrmann, H.J., 2002b. Minimal model for aeolian sand dunes. Phys. Rev. E 66, 031302.

Kroy, K., Fischer, S., Obermayer, B., 2005. The shape of barchan dunes. J. Phys. Condens. Matter 17, S1229–S1235.

Landau, L., Lifchitz, E., 1990. Theory of Elasticity. Mir, Moscow.

Leenders, J.K., van Boxel, J.H., Sterk, G., 2005. Wind forces and related saltation transport. Geomorphology 71, 357–372.

Le Louvetel-Poilly, J., Bigillon, F., Doppler, D., Vinkovic, I., Champagne, J.-Y., 2009. Experimental investigation of ejections and sweeps involved in particle suspension. Water Resour. Res. 45, W02416.

Lettau, K., Lettau, H.H., 1978. Experimental and micro-meteorological field studies of dune migration. In: Lettau, H.H., Lettau, K. (Eds.), Exploring the World's Driest Climate. University of Wisconsin-Madison, Institute for Environmental Studies, IES Report 101, pp. 110–147.

Liu, X., Dong, Z., 2004. Experimental investigation of the concentration profile of a blowing sand cloud. Geomorphology 60, 371–381.

Long, J.T., Sharp, R.P., 1964. Barchan dune movement in imperial valley, California. Geol. Soc. Am. 75, 149–156.

Lovejoy, S., Schertzer, D., 2010. Towards a new synthesis for atmospheric dynamics: space-time cascades. Atmos. Res. 96, 1–5.

Fernandez Luque, R., van Beek, R., 1976. Erosion and transport of bed-load sediment. J. Hydraul. Res. 14, 127–144.

Matas, J.P., Morris, J.F., Guazzelli, E., 2004. Lateral forces on a sphere oil & gas science and technology. Rev. IFP 59, 59–70.

McEwan, I.K., Willetts, B.B., 1991. Numerical model of the saltation cloud. Acta Mech. 1 (Suppl.), 53–66.

McEwan, J.K., Willetts, B.B., Rice, M.A., 1992. The grain/bed collision in sand transport by wind. Sedimentology 39, 971–981.

McEwan, J.K., Willetts, B.B., 1993. Sand transport by wind: a review of the current conceptual model. Geol. Soc. Spec. Publ. 72, 7–16.

Moraga, F.J., Bonetto, F.J., Lahey, R.T., 1999. Lateral forces on spheres in turbulent uniform shear flow. Int. J. Multiphase Flow 25, 1321–1372.

Mordant, N., Pinton, J-F., 2000. Velocity measurement of a settling sphere. Eur. Phys. J. B 18, 343–352.

Nalpanis, P., Hunt, J.C.R., Barrett, C.F., 1993. Saltating particles over flat beds. J. Fluid Mech. 251, 661–685.

Namikas, S.L., 2003. Field measurement and numerical modeling of aeolian mass flux distributions on a andy beach. Sedimentology 50, 303–326.

Nickling, W.G., 1978. Eolian sediment transport during dust storms: Slims River valley, Yukon Territory. Can. J. Earth Sci. 15, 1069–1084.

Nickling, W.G., McKenna Neuman, C., 2009. Aeolian sediment transport. In: Parsons, A., Abrahams, A.D. (Eds.), Geomorphology of Desert Environments, Part VII. Springer, New York, pp. 517–555.

Owen, P.R., 1964. Saltation of uniform grains in air. J. Fluid Mech. 20, 225–242.

Prandtl, L., 1925. Bericht über Untersuchungen zur ausgebildeten Turbulenz. Z. Angew. Math. Mech. 5, 136–139.

Prigozhin, L., 1999. Nonlinear dynamics of aeolian sand ripples. Phys. Rev. E 60, 729.

Pye, K., Tsoar, H., 1990. Aeolian Sand and Sand Dunes. Unwin Hyman, London.

Quartier, L., Andreotti, B., Daerr, A., Douady, S., 2000. Dynamics of a grain on a sandpile model. Phys. Rev, E 62, 8299–8307.

Rasmussen, K.R., Iversen, J.D., Rautaheimo, P., 1996. Saltation and wind flow interaction in a variable slope wind tunnel. Geomorphology 17, 19–28.

Rasmussen, K.R., Mikkelsen, H.E., 1991. Wind tunnel observations of aeolian transport rates. Acta Mech. 1 (Suppl.), 135–144.

Rasmussen, K.R., Sorensen, M., 2008. Vertical variation of particle speed and flux density in aeolian saltation: measurement and modeling. J. Geol. Res. 113, F02S12. doi:10.1029/2007JF000774.

Raupach, M.R., Antonia, R.A., Rajagopalan, S., 1991. Rough-wall turbulent boundary layers. Appl. Mech. Rev. 44, 1–25.

Richards, K.J., 1980. The formation of ripples and dunes on an erodible bed. J. Fluid Mech. 99, 597–618.

Rioual, F., Valance, A., Bideau, D., 2000. Experimental study of the collision process of a grain on a two-dimensional granular bed. Phys. Rev. E 62, 2450–2459.

Rubinows, I., Keller, J.B., 1961. The transverse force on a spinning sphere moving in a viscous fluid. J. Fluid Mech. 11, 447–459.

Sarre, R.D., 1987. Aeolian sand transport. Prog. Phys. Geogr. 11, 157–182.

Sauermann, G., Kroy, K., Herrmann, H.J., 2001. A phenomenological dynamic saltation model for dune formation. Phys. Rev. E 64, 031305.

Schwämmle, V., Herrmann, H.J., 2005. A model of barchan dunes including lateral shear stress. Eur. Phys. J. E 16, 57–65.

Schlichting, H., Gersten, K., 2000. Boundary Layer Theory, eigth ed. Springer-Verlag, Berlin.

Shao, Y., 2000. Physics and Modelling of Wind Erosion. Kluwer Academic Publishers.

Shao, Y., Raupach, M.R., 1992. The overshoot and equilibration of saltation. J. Geophys. Res. 97, 20559–20564.

Sherman, D.J., 1992. An equilibrium relationship for shear velocity and apparent roughness length in aeolian saltation. Geomorphology 5, 419–431.

Sherman, D.J., Farrell, E.J., 2008. Aerodynamic roughness lengths over movable beds: comparison of wind tunnel and field data. J. Geophys. Res. 113, F02S08.

Slattery, M.C., 1990. Barchan migration on the Kuiseb river delta, Namibia. S. Afr. Geogr. J. 72, 5–10.

Sørensen, M., 1991. An analytic model of wind-blown sand transport. Acta Mech. 1 (Suppl.), 67–81.

Sørensen, M., 2004. On the rate of aeolian sand transport. Geomorphology 59, 53–62.

Sørensen, M., McEwan, I.K., 1996. On the effect of mid-air collisions on aeolian saltation. Sedimentology 43, 65–76.

Spies, P.-J., McEwan, I.K., 2000. Equilibration of saltation. Earth Surf. Processes Landforms 25, 437–453.

Stull, R.B., 1988. An Introduction to Boundary Layer Meteorology. Kluwer Academic Publishers.

Svasek, J.N., Terwindt, J.H.J., 1974. Measurements of sand transport by wind on a natural beach. Sedimentology 21, 311–322.

Terzidis, O., Claudin, P., Bouchaud, J.-P., 1998. A model for ripple instabilities in granular media. Eur. Phys. J. B 5, 245.

Tomiyama, A., 2010. Single bubbles in stagnant liquids and in linear shear flows (Preprint).

Ungar, J.E., Haff, P.K., 1987. Steady state saltation in air. Sedimentology 34, 289–299.

Valance, A., Langlois, V., 2005. Ripple formation over a sand bed submitted to a laminar shear flow. Eur. Phys. J. B 43, 283–294.

Van der Hoven, I., 1957. Power spectrum of horizontal wind speed in the frequency range from. 0007 to 900 cycles per hour. J. Meteorol. 14, 160–164.

Van Boxel, J.H., Sterk, G., Arens, S.M., 2004. Sonic anemometers in aeolian sediment transport research. Geomorphology 59, 131–147.

Werner, B.T., 1990. A steady-state model of wind-blown sand transport. J. Geol. 98, 1–17.

White, B.R., 1979. Soil transport by winds on Mars. J. Geophys. Res. 84, 4643–4651.

White, B.R., 1982. Two-phase measurements of saltating turbulent boundary layer flow. Int. J. Multiphase Flow 8, 459–473.

White, B.R., Mounla, H., 1991. An experimental study of Froude number effect on wind-tunnel saltation. Acta Mech. 1 (Suppl.), 145–157.

White, B.R., Schulz, J.C., 1977. Magnus effect in saltation. J. Fluid Mech. 81, 497–512.

Willetts, B., 1983. Transport by wind of granular material of different grain shapes and densities. Sedimentology 30, 669–679.

Willetts, B.B., McEwan, J.K., Rice, M.A., 1991. Initiation of motion of quartz sand grains. Acta Mech. 1 (Suppl.), 123–134.

Willetts, B.B., Murray, C.G., 1981. Lift exerted on stationary spheres in turbulent flow. J. Fluid Mech. 105, 487–505.

Willetts, B.B., Rice, M.A., Swaine, S.E., 1982. Shape effects in aeolian grain transport. Sedimentology 29, 409–417.

Williams, G., 1964. Some aspects of aeolian saltation load. Sedimentology 3, 257–287.

Yalin, M.S., Karahan, E.J., 1979. Inception of sediment transport. J. Hydraul. Div. 105, 1433–1443.

Yizhaq, H., Balmforth, N.J., Provenzale, A., 2004. Blown by wind: nonlinear dynamics of aeolian sand ripples. Physica D 195, 207–228.

Zheng, X., 2009. Mechanics of Wind-blown Sand Movements. Springer-Verlag, Berlin.

Zingg, A.W., 1953. Wind tunnel studies of movement of sedimentary material. Proc. Fifth Hydraulic Conference Bull., vol. 34, pp. 111–134.